Journal of Molecular Structure 1292 (2023) 136079

Contents lists available at ScienceDirect

Journal of Molecular Structure

journal homepage: www.elsevier.com/locate/molstr

Fe_3O_4@SiO_2@TDI@DES: A novel magnetically separable catalyst for the synthesis of oxindoles

Prasad Swami [a], Sanket Rathod [b], Prafulla Choudhari [b], Devashree Patil [c], Ajinkya Patravale [d], Yogesh Nalwar [e], Sandeep Sankpal [a,*], Shankar Hangirgekar [a,*]

[a] Department of Chemistry, Shivaji University, Kolhapur 416004, Maharashtra, India
[b] Department of Pharmaceutical Chemistry, Bharati Vidyapeeth College of Pharmacy, Kolhapur 416013, Maharashtra, India
[c] Department of Biotechnology, Shivaji University, Kolhapur 416004, Maharashtra, India
[d] Department of Chemistry, Vivekanand College, Kolhapur 416003, Maharashtra, India
[e] Department of Chemistry, Toshniwal A.C.S. College, Sengaon 431542, Maharashtra, India

ARTICLE INFO

Keywords:
Sustainable chemistry
Deep eutectic solvent
Heterogeneous catalyst
Magnetic nanoparticles
Oxindole

ABSTRACT

A novel magnetically separable Fe_3O_4@SiO_2@TDI@DES catalyst was synthesized by covalent anchoring of Deep Eutectic Solvent [DES; oxalic acid: choline chloride] on Fe_3O_4@SiO_2@TDI magnetic nanoparticles. The structure of the catalyst was confirmed by FT-IR, XRD, EDX, TGA-DTA, VSM, FE-SEM, and HR-TEM analyses. The synthesized magnetically separable catalyst demonstrated excellent catalytic activity in the terms of yield and reaction time for the synthesis of 2,2′-(2-oxoindoline-3–3diyl)bis(1H-indene-1,3(2*H*)-dione) from 1,3-indendione and isatin. In addition, the catalyst could be reused for five runs without significant loss of catalytic activity. The synthesized oxindole derivatives showed promising in vitro antioxidant activities which were further supported by molecular docking and molecular dynamic (MD) simulation studies.

1. Introduction

Consequent to severe environmental pollution and stringent rules, the creation of greener methodologies have had a significant influence in modern synthetic chemistry [1–2]. Particularly, the developments of greener methodologies using nontoxic and biocompatible catalysts have received noteworthy significance in the development of sustainable processes [3–4]. Implementation of sustainable methodologies for industrial scale synthesis using convenient and less harmful energy sources is the prime objective to cope with present global pollution [5–6].

In this context, deep eutectic solvent (DES) have attracted researchers in the last few decades for their range of envisaged applications in organic reactions [7–8]. The catalytic efficiency of DES has been explored in various organic reactions owing to their important features such as biodegradability, high stability, low vapor pressure, high selectivity, and low cost of synthesis [9–11]. However, catalytic applications of DES in synthetic conversions are hampered considerably due to the need for a sizeable amount of DES, the tedious recovery process, and loss during isolation [12]. Owing to these limitations, the effective greenness of DES is lessened considerably.

To circumvent this issue, immobilization DES on heterogeneous supports have been introduced in recent years and revealed to play a promising catalytic role in organic reactions [13,32]. Among the solid supports, magnetic nanoparticles (MNPs) are found to be an excellent support for the covalent immobilization of homogeneous catalysts [14]. Due to the uniform distribution of catalytic active sites on the surface and the ease of magnetic separation from the reaction mixture, covalent anchoring of DES on Fe_3O_4 MNPs have shown an excellent catalytic performance in a variety of organic transformations [15–17].

On the other hand, oxindole is one of the important classes of nitrogen heterocycles prevalent in mammal body fluids, tissues, and natural products [18]. In this context, oxindole derivatives have attracted the attention of researchers as these exhibit significant biological activities such as antibacterial, antifungal [19], antiviral [20], antimicrobial [21], antileishmanial [22], and antioxidative [23] activities. Also, some of the oxindole derivatives are being investigated primarily for anticancer treatment [24] shown in Fig. 1.

The commercial approach for oxindole synthesis involves acid-catalyzed condensation of arenes with isatin. The synthesis of oxindoles using *p*-TSA and ChCl/glycerol has been reported earlier [25],

* Corresponding authors.
E-mail address: sph.chem@unishivaji.ac.in (S. Hangirgekar).

https://doi.org/10.1016/j.molstruc.2023.136079
Received 9 December 2022; Received in revised form 17 March 2023; Accepted 19 June 2023

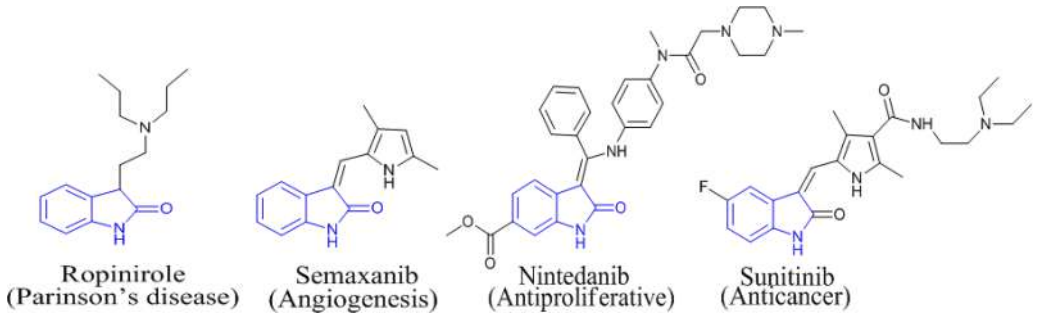

Fig. 1. Biologically active naturally obtained oxindole derivatives.

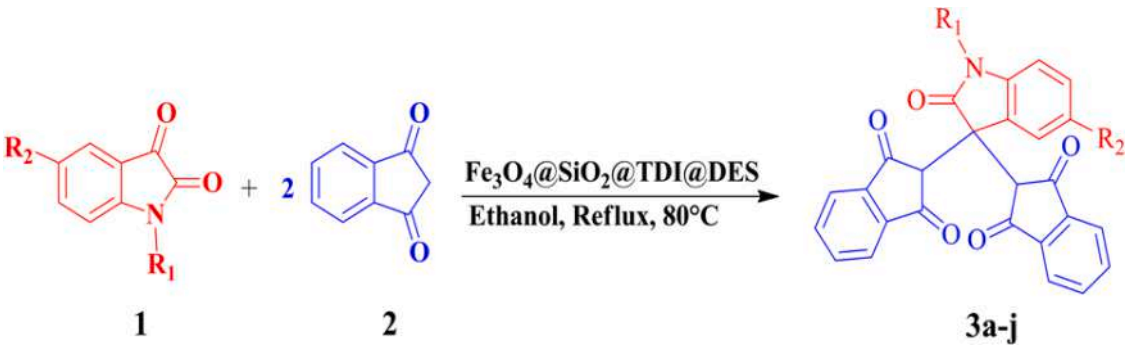

Scheme 1. Fe_3O_4@SiO_2@TDI@DES catalyzed synthesis of oxindole.

however, lower yield, longer reaction time, difficult to recycle, and poor selectivity have been the limiting factors. With this rationale, we demonstrate an efficient and sustainable method for the synthesis of oxindoles via a one-pot pseudo-three component reaction of 1,3-indendione and isatin catalyzed by Fe_3O_4@SiO_2@TDI@DES magnetic catalyst in ethanol under reflux condition. In addition, the synthesized oxindoles (Scheme 1) have been tested for their antioxidant activities and further supported by molecular docking study as well as molecular dynamic (MD) simulation.

2. Experimental

2.1. General

The required chemicals were purchased from Spectrochem and Sigma-Aldrich chemical company and used without any further purification. The progress of reactions was monitored by thin-layer chromatography (TLC) on a silica-coated aluminum plate. Melting points of synthesized compounds were measured in the open capillary. ^1H and ^{13}C NMR were recorded on Bruker AC (300 MHz and 400 MHz) at operating frequencies 75 and 100 MHz using DMSO-d_6 as a solvent and TMS (tetramethylsilane) as an internal standard. The mass of synthesized compounds was recorded using Waters ZQ-4000 (ESI-MS) in positive ion mode. FT-IR spectra were recorded using a KBr pellet with a Bruker IR spectrophotometer in the range 4000–400 cm^{-1}. XRD pattern of the synthesized materials was recorded using Ultima IV, Rigaku Corporation. The thermal stability study of the catalyst was performed using a TGA, Netzsch STA 409 under a nitrogen atmosphere at the flow rate of 20 mL $min.^{-1}$ with a heating rate of 10 °C $min.^{-1}$ from 40 °C to 700 °C. The chemical composition of the Fe_3O_4@SiO_2@TDI@DES was determined using EDX on JSF-7600F. The surface morphology of the material was studied using FE-SEM on TESCAN, Mira3, and HR-TEM on Tecnai G2, F30. Magnetic properties of Fe_3O4@SiO_2@TDI@DES nanocomposite were measured using a VSM of the Lakeshore 7410S model.

2.2. Catalyst preparation

2.2.1. Preparation of Fe_3O_4

A co-precipitation method was preferred to prepare Fe_3O_4 magnetic nanoparticles (NPs) by taking $FeCl_3{\cdot}6H_2O$ and $FeCl_2{\cdot}4H_2O$ as starting precursors. An aqueous solution of Fe^{+3} and Fe^{+2} was prepared in a molar ratio of 2:1 and kept for heating at 50 °C for 10 min. Then, aqueous ammonia solution was added slowly to maintain pH 11 and stir continuously for 2 h. The obtained black precipitate of Fe_3O_4 was separated using an external magnet and washed thoroughly with distilled water till the solution becomes neutral. Further, Fe_3O_4 was rinsed with ethanol and then kept for drying at 50 °C in the oven [26–27].

2.2.2. Preparation of Fe_3O_4@SiO_2 nanoparticles

The surface Fe_3O_4 MNPs were modified by silica layer using tetraethyl orthosilicate (TEOS) by employing a sol-gel process to avoid oxidation and aggregation. The Fe_3O_4 MNPs (0.25 g) were added to a mixture of ethanol and water (40 mL + 15 mL) and then dispersed uniformly in an ultrasonicator. The resultant solution was diluted with 4.5 mL conc. NH_4OH, and then TEOS (1 mL) slowly added with stirring. After the complete addition of TEOS, the above solution was kept for stirring for 12 h at room temperature. After completion of the reaction, the precipitate of Fe_3O_4@SiO_2 was separated by applying an external magnetic field. Using water and ethanol the Fe_3O_4@SiO_2 MNPs were rinsed utterly and kept in a vacuum oven for drying at 50 °C [28–29].

2.2.3. Preparation of Fe_3O_4@SiO_2@TDI nanoparticles

Fe_3O_4@SiO_2@TDI was prepared from a reported procedure with slight modification [30]. The synthesized Fe_3O_4@SiO_2 (1.0 g) was dispersed in 50 mL dry toluene and 1.40 g of TDI was mixed into it ultrasonically for 10–15 min. The reaction mixture was kept stirring for 6 h. The reaction between well-dispersed Fe_3O_4@SiO_2 and TDI resulted in the formation of desired Fe_3O_4@SiO_2@TDI MNPs under ultrasonic condition. To remove the physisorbed and unreacted TDI molecules, the Fe_3O_4@SiO_2@TDI was centrifuged and rinsed with dry toluene, and

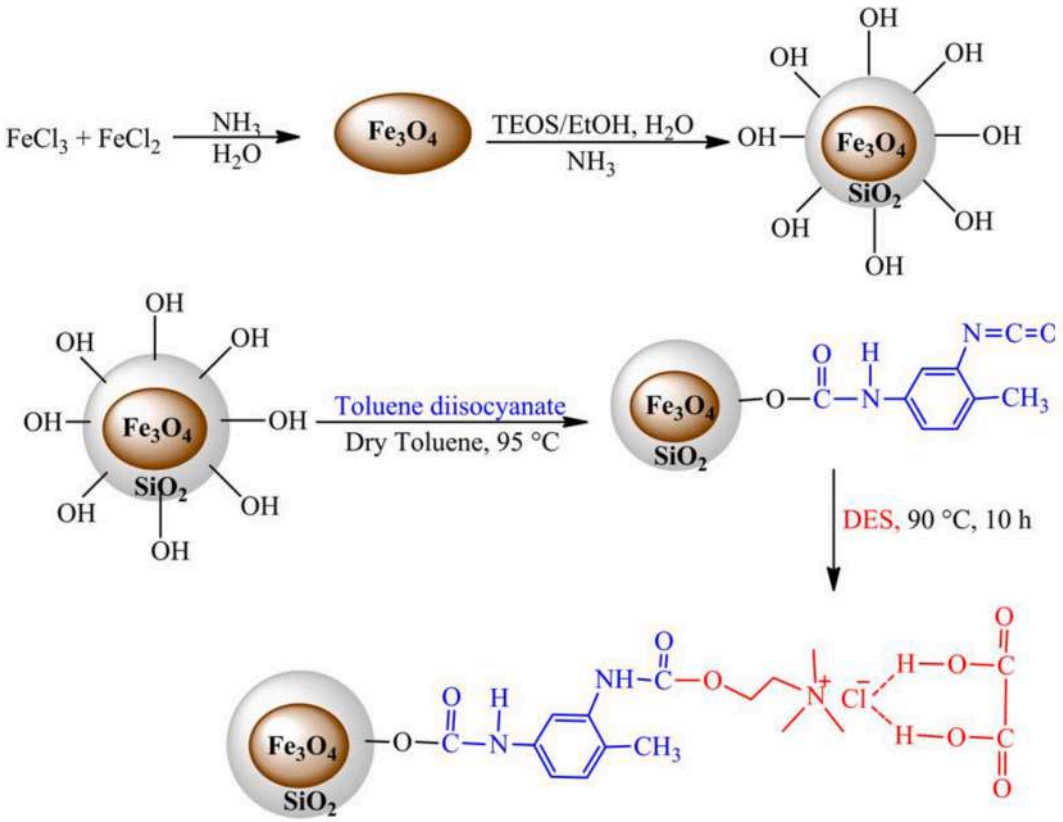

Scheme 2. Synthesis of magnetically separable Fe_3O_4@SiO_2@TDI@DES catalyst.

then vacuum dried at 80 °C for 24 h [30].

2.2.4. Preparation of DES

In a round bottom flask, the mixture of choline chloride and oxalic acid was placed in a 1:1 molar ratio and heated up to 100 °C to get a clear, transparent, homogeneous DES, choline chloride: oxalic acid with 100% atom economy [31].

2.2.5. Synthesis of DES functionalized Fe_3O_4 @SiO_2@TDI@DES

A mixture of Fe_3O_4@SiO_2@TDI (0.600 g) and DES [choline chloride: oxalic acid] (0.600 g) was placed in a 50 mL round bottom flask and stirred for 18 h at 100 °C. After completion of the reaction, 10 mL water was added to the reaction mixture to remove unreacted DES, and then ethanol was used to rinse the desired Fe_3O_4@SiO_2@TDI@DES. The solid catalyst was oven dried at 50 °C for 10 h [32]. The schematic diagram for the synthesis of Fe_3O_4@SiO_2@TDI@DES catalyst is shown in Scheme 2.

2.3. General procedure for preparing oxindoles

A mixture of 1,3-indendione (2 mmol), isatin (1 mmol), and Fe_3O_4@SiO_2@TDI@DES (0.015 g) in 5 mL ethanol was stirred at 80 °C till completion of the reaction as monitored by thin-layer chromatography (TLC). After completion of the reaction, the catalyst was separated easily by an external magnet. The pure product was obtained by washing the precipitate with hot EtOH. The structure of unknown oxindoles was ascertained by spectroscopic techniques such as IR, ^{1}H, and ^{13}C NMR and mass spectrometry.

2.4. In silico studies

2.4.1. Protein and ligand preparation

The previously reported 3D Crystal structure of aromatase with PDB: 3s79 having 2.75 Å resolution was downloaded from the RCSB Protein data bank (https://www.rcsb.org/) [33]. The further downloaded protein structure was cleaned by removing water molecules and previously bound ligand groups and the addition of polar hydrogen atoms to the cleaned protein was done to define the correct ionization as well as tautomeric states of amino acid residues. Thereafter prepared protein structure was validated using the PROCHECK tool to determine the quality of the protein [34].

The binding pocket was predicted using CASTp 3.0 server [35]. These identified active binding sites were used for the identification of the best ligand binding site in the respective target protein. The structures of synthesized compounds in **Table S1** (Shown in supporting information) have been drawn and saved as mol2 files by using ACD/ChemSketch software (https://www.acdlabs.com/) and thereafter imported into BIOVIA Discovery Studio (DS) 2020 to optimize by adding hydrogen atoms and convert into PDB files format for further *in-silico* studies.

2.4.2. Molecular docking analysis

Molecular docking studies were performed to check the binding sites and interactions occurring between the synthesized compounds and the target protein (PDB: 3s79). Molecular docking was performed using PyRx 0.8 software [36]. The PDB file format of 3s79 as a macromolecule and the SDF file format of all synthesized compounds were imported in PyRx. Synthesized ligands were then converted to PDBQT format using the Open Babel plugin of PyRx and further used for molecular docking. The grid box for the PDB ID: 3s79 was selected in the Vina workspace of PyRx to cover the binding site residues, with center X: 83.3339, Y: 50.1222, Z: 46.4506 and dimensions X: 59.8626 Å, Y: 71.3579 Å, Z: 50.5436 Å. The docking procedure was carried out on the AutoDockVina plugin of PyRx. The exhaustiveness was set to default at 8. Nine different poses (conformations) were predicted for each ligand with the selected target protein displayed. Further, the best pose with minimum binding

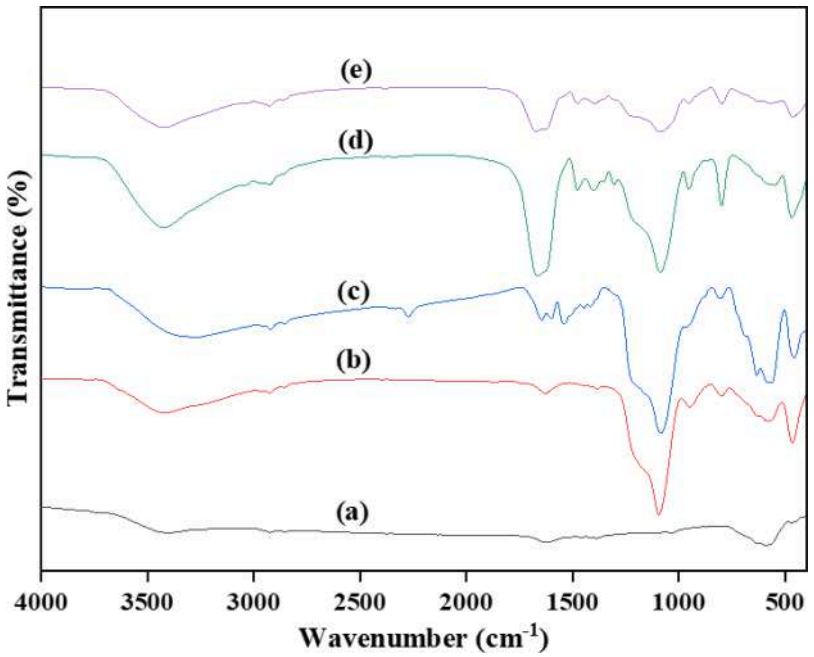

Fig. 2. FT-IR spectra of (a) Fe_3O_4, (b) Fe_3O_4@SiO_2, (c) Fe_3O_4@SiO_2@TDI, (d) Fe_3O_4@SiO_2@TDI@DES (e) Fe_3O_4@SiO_2@TDI@DES after 5th run.

energy was selected for each ligand. Docking interaction visualization and analysis of saved pose were carried out using the BIOVIA DS 2020.

2.4.3. Drug-likeness and in-silico ADMET properties

The evaluation of drug-likeness and pharmacokinetic properties of the synthesized compounds was done by the computational method using SwissADME and pkCSM servers [37–38]. Drug-likeness of compounds was predicted based on various rules such as Lipinski, Ghose, Veber, Egan, and Muegge, and their synthetic accessibility [39]. Pharmacokinetic ADMET (absorption, distribution, metabolism, excretion, and toxicity) properties were studied to evaluate the activity of synthesized compounds within the human body [40]. The oral bioavailability of compounds showing good permeability of membrane and hydrophobicity of drug molecules is indicated by the Log P, TPSA, MW, HBA, and HBD values [41].

2.4.4. Molecular dynamic simulation

Protein-ligand complex having high binding affinity was subjected to Molecular dynamics (MD) simulation by using WebGRO and CABS-flex 2.0 [42–43]. WebGRO tool is based on GROMACS and the GROMOS96 43a1 force field was chosen to perform this simulation [44]. To perform MD simulation, the protein (PDB ID: 3s79) structure file was uploaded on WebGRO in PDB format. The PRODRG 2.5 server was used to prepare the ligand topology file [45]. The water model was selected as SPC with a triclinic box. Energy minimization parameters were set to default at the steepest descent algorithm with 2000 steps. The simulation was neutralized and performed in the presence of 0.15 M NaCl with a constant temperature of 300 K and pressure of 1.0 bar. The equilibration process was done after energy minimization using the NVT/NPT. After equilibration, all other parameters were set to default, and the final production MD simulation was performed for 100 ns to check the stability of the protein-ligand complex. Complex stability was evaluated by analyzing the root mean square deviation (RMSD) and root mean square fluctuation (RMSF) of the obtained trajectory. RMSD profiles of the complex were evaluated through the WebGRO server and RMSF was evaluated through CABS-flex 2.0 with default settings.

2.5. Antioxidant assay

2.5.1. Determination of antioxidant activity by DPPH- scavenging assay

The method of Patil et al., (2020) was adopted to carry out the assay [46]. Using 1,1-diphenyl-2-picrylhydrazyl (DPPH) radical scavenging, the investigated compound's free radical scavenging activity was calculated. 2 mL of 1.0 mmol L^{-1} DPPH radical solution produced in methanol and 1 mL of synthesized chemicals (100 μg) make up the reaction mixture. The solution was quickly mixed, then incubated at 37 °C for 20 min. in the dark. A decrease in absorption at 517 nm was used to evaluate the reduction of DPPH radical in each solution using a UV–Vis spectrophotometer. The positive control was ascorbic acid. The percentage of radical scavenging (%) was subsequently calculated as equation 1.

% Radical scavenging = Absorbance of control - Absorbance of sample/control X 100

2.6. Spectral data of unknown compounds

2,2́-(5-chloro-2-oxoindoline-3,3-diyl)bis(1H-indene-1,3(2H)-dione) (3 g): (*Table 2, entry 7):*

Gray solid; Mp: 250–252 °C; FT-IR (KBr): 761, 1267, 1602, 1709, 2908, 3084, 3403; ^{1}H NMR (400 MHz, DMSO-d_6): δ 4.76 (2H, s, CH), 6.71 (1H, d, J = 8 Hz, ArH), 6.78 (1H,d, J = 2 Hz, ArH), 7.01–7.04 (1H, m, J = 12 Hz, ArH), 7.78–7.88 (8H, m, ArH), 10.67 (1H, s, -NH); ^{13}C NMR (100 MHz, DMSO-d_6): δ 52.51, 111.62, 123.16, 123.29, 126.49, 129.08, 130.10, 136.18, 136.43, 141.96, 142.14, 175.86; LC-MS (ESI): m/z = 456 [M + 1].

2,2́-(5-iodo-2-oxoindoline-3,3-diyl)bis(1H-indene-1,3(2H)-dione) (3 h): (*Table 2, entry8):*

Gray solid; Mp: 262–264 °C; FT-IR (KBr): 758, 1264, 1592, 1709, 2921, 3080, 3321, 3354; ^{1}H NMR (400 MHz, DMSO-d_6): δ 4.73 (2H, s, CH), 6.56 (1H, q, J = 10 Hz, ArH), 7.07 (1H,s, ArH), 7.34 (1H, d, J = 8 Hz, ArH), 7.81–7.82 (8H, m, J = 6 Hz, ArH), 10.65 (1H, d, NH); ^{13}C NMR (100 MHz, DMSO-d_6): δ 52.27, 84.16, 112.67, 123.11, 123.17, 130.80, 131.60, 136.14, 136.38, 137.82, 142.15, 142.94, 175.56 LC-MS (ESI): m/z = 548 [M + 1].

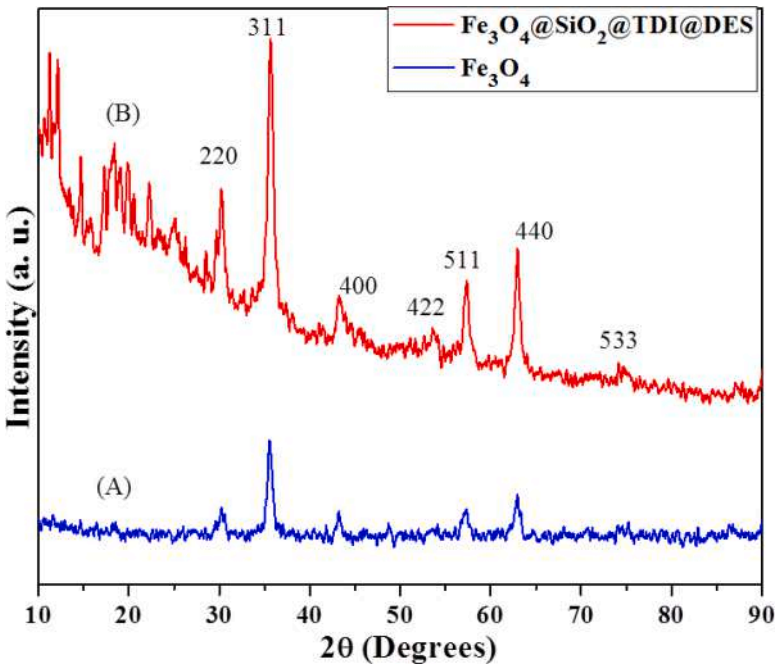

Fig. 3. XRD patterns of (a) Fe_3O_4 (b) Fe_3O_4@SiO_2 and (c) Fe_3O_4@SiO_2@TDI@DES.

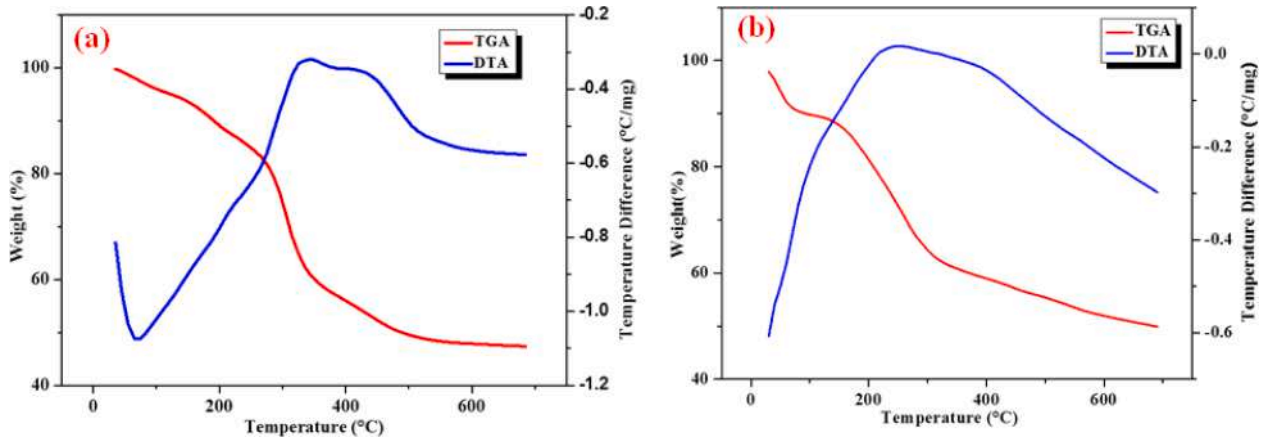

Fig. 4. TGA and DTA curve of (a) Fe_3O_4@SiO_2@TDI@DES, (b) Reused Fe_3O_4@SiO_2@TDI@DES catalyst.

2,2́-(1-(4-chlorobenzyl)−2-oxoindoline-3,3-diyl)bis(1H-indene-1,3 (2H)-dione) (3i): (Table 2, entry 9):

Gray solid; Mp: 234–236 °C; FT-IR (KBr): 762, 1255, 1598, 1703, 2884, 3010; ^{1}H NMR (400 MHz, DMSO-d_6): δ 4.65(2H, s, CH), 4.76(2H, s, CH2), 6.34–6.56(1H, m, ArH), 6.67–6.79(1H, m, ArH), 6.87–7.37(7H, m, ArH), 7.74–8.20(7H, m, ArH); ^{13}C NMR (100 MHz, DMSO-d_6): δ 43.46, 51.95, 53.72, 92.05, 109.47, 122.96, 123.14, 128.60, 128.78, 129.20, 135.86, 136.15, 142.20, 148.60, 174.67, 189.28; LC-MS (ESI): $m/z = 546$ [$M + 1$].

2,2́-(1-(4-methylbenzyl)−2-oxoindoline-3,3-diyl)bis(1H-indene-1,3 (2H)-dione) (3j): (Table-2, entry 10):

Gray solid; Mp: 242–244 °C; FT-IR (KBr): 758, 1256, 1600, 1702, 2820, 2966; ^{1}H NMR (400 MHz, DMSO-d_6): δ 2.16 (3H, s, CH_3), 4.62 (2H, s, CH), 4.74 (2H, s, CH_2), 6.50 (1H, d, ArH), 6.67 (1H, d, ArH), 6.86–7.15 (7H, m, ArH), 7.44–7.86 (7H, m, ArH); ^{13}C NMR (100 MHz, DMSO-d_6): δ 21.11, 43.71, 52.13, 109.71, 122.76, 123.05, 123.12, 127.25, 127.31, 127.43, 127.57, 129.16, 129.24, 129.37, 129.42, 129.88, 132.46, 136.07, 136.37, 136.88, 140.00, 142.32, 143.67, 174.51, 191.17, 192.14; LC-MS (ESI): $m/z = 526$ [$M + 1$].

3. Results and discussion

3.1. Characterization of Fe_3O_4@SiO_2@TDI@DES

The synthesized Fe_3O_4@SiO_2@TDI@DES magnetic catalyst was characterized by various tools such as Fourier transform-infrared (FT-IR) spectroscopy, X-ray diffraction spectroscopy (XRD), thermogravimetric analysis (TGA-DTA), energy dispersive X-ray spectroscopy (EDX), field emission scanning electron microscopy (FE-SEM), high-resolution transmission electron microscopy (HR-TEM), and vibrating sample magnetometry (VSM) analyses.

3.1.1. Fourier transform-infrared (FT-IR) spectra

The FT-IR spectrum of Fe_3O_4@SiO_2@TDI@DES was recorded in the range from 400 to 4000 cm^{-1} (Fig. 2).

The FT-IR spectra in Fig. 2 show absorption at 589 cm^{-1} corresponding to Fe-O stretching [47], whereas the stretching vibration of a hydroxyl group O—H is appeared at 3410 cm^{-1}. The bending vibration of adsorbed water is responsible for the appearance of the stretching band at 1626 cm^{-1} (Fig. 2a). The symmetric and asymmetric stretching

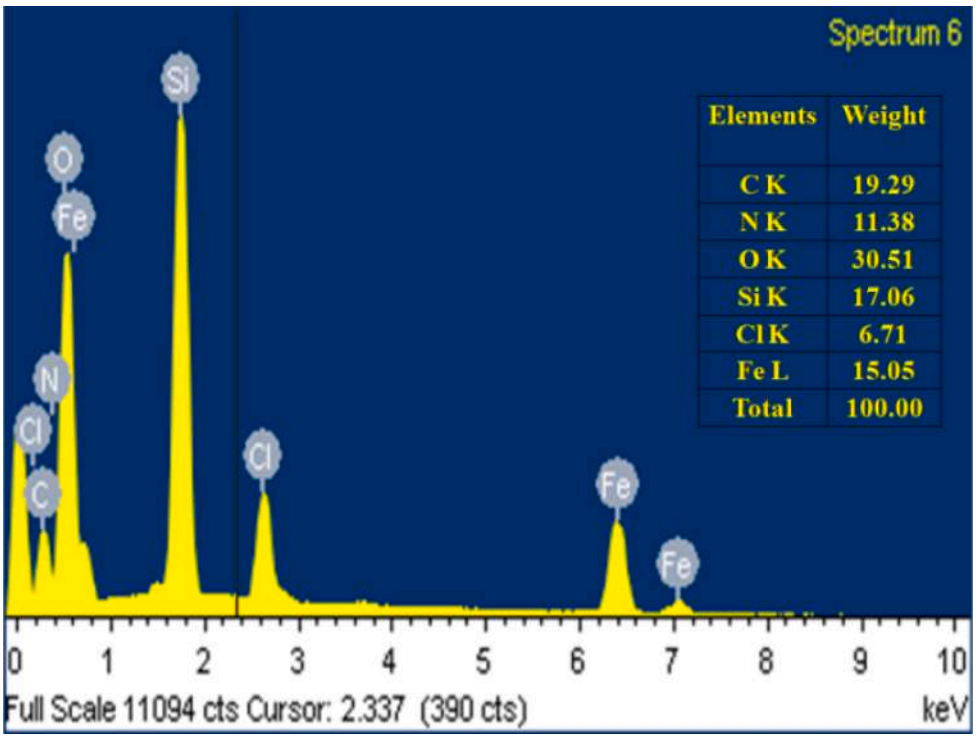

Fig. 5. EDX patterns of Fe_3O_4@SiO_2@TDI@DES.

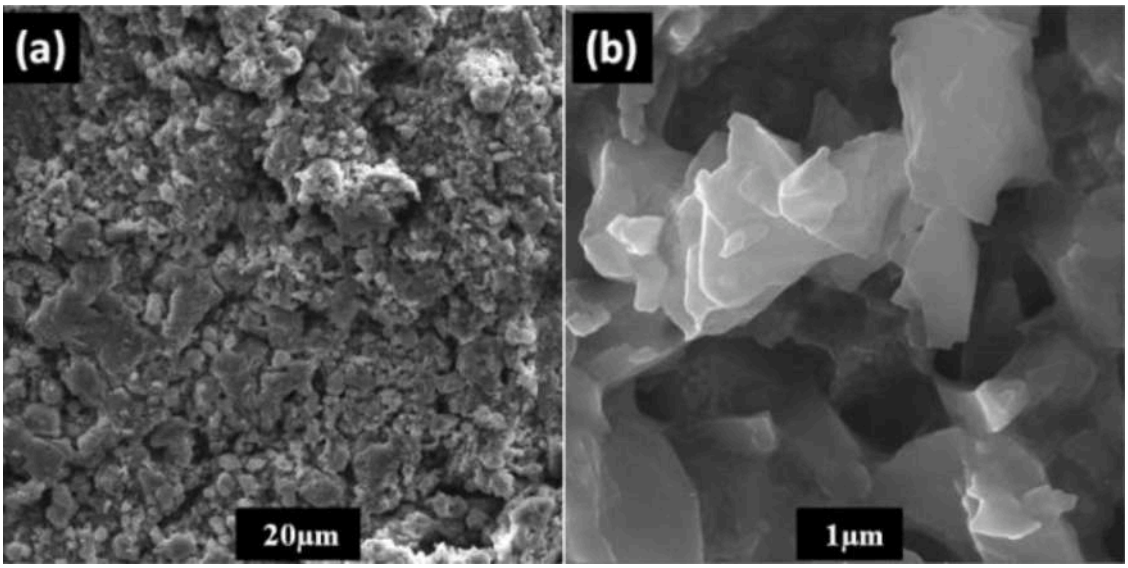

Fig. 6. FE-SEM images (a, b) of Fe_3O_4@SiO_2@TDI@DES.

vibrations of the Si–O–Si bond appeared at 948 cm^{-1} and 1093 cm^{-1} respectively (Fig. 2b) [48–49]. The anchoring of the TDI molecule on the surface of Fe_3O_4@SiO_2 was confirmed based on stretching vibrations at 2273 cm^{-1}, 1630 cm^{-1}, and 1545 cm^{-1} corresponding to orthoisocyanate group, carbonyl stretching and C = C stretching of the phenyl ring (Fig. 2c) [50]. The disappearance of the band at 2273 cm^{-1} corresponding to orthoisocyanate stretching corroborates the attachment of DES to the isocyanate group of TDI. Also due to the hydrogen bonding present between oxalic acid and choline chloride, the value of C = O stretching decreases up to 1662 cm^{-1} (Fig. 2d). The FT-IR spectrum of Fe_3O_4@SiO_2@TDI@DES after 6th run found to be unchanged indicating structural integrity of the catalyst (Fig. 2e).

3.1.2. *X-ray diffraction (XRD) spectra*

The crystalline structure of the synthesized NPs was examined using the X-ray powder diffraction technique. As shown in Fig. 3, diffraction peaks at 30.1 (220), 35.4 (311), 43.2 (400), 53.6 (422), 57.1 (511), and 63 (440) explicitly show the formation of the Fe_3O_4 NPs and the data was in good agreement with the Joint Committee on Powder Diffraction Standards (JCPDS card no.01–071–6336) [51–52]. The broad diffraction peaks at ~20–23 correspond to the amorphous state of SiO_2 shell surrounding the Fe_3O_4 nanoparticles (Fig. 3b). Even after functionalization, the diffraction pattern and location of the characteristic peaks were observed in Fe_3O_4@SiO_2@TDI@DES (Fig. 3c) confirming that the crystalline spinel structure is retained.

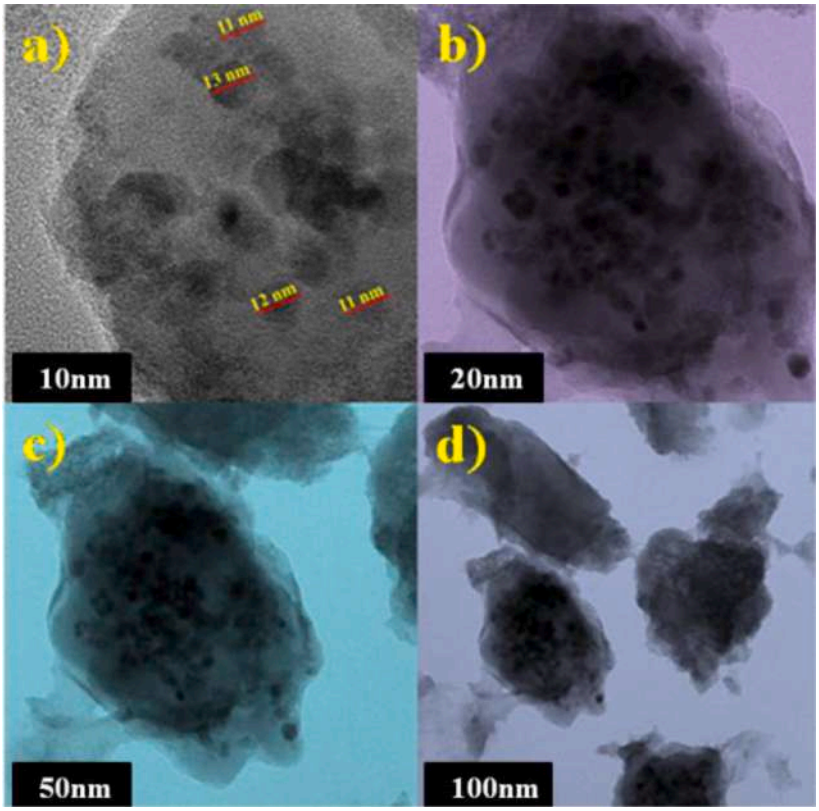

Fig. 7. TEM images of Fe_3O_4@SiO_2@TDI@DES.

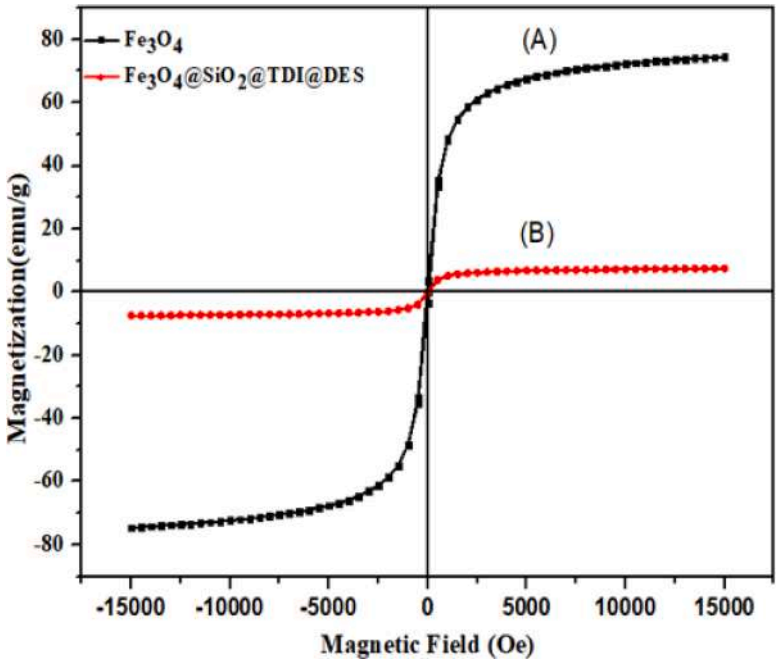

Fig. 8. Magnetization curve (a) Fe_3O_4 and (b) Fe_3O_4@SiO_2@TDI@DES.

3.1.3. Thermogravimetric analysis-Differential thermal analysis (TGA-DTA)

Thermogravimetric analysis (TGA) and differential thermal analysis (DTA) experiment of Fe_3O_4@SiO_2@TDI@DES was carried out in an N_2 atmosphere at a heating rate of 10 °C $min.^{-1}$ as shown in Fig. 4a. The first step of the thermogram in TGA and deep endotherm peak in DTA occurs within the temperature range of 25–100 °C (3.95%) due evaporation of the physically adsorbed water molecules. The second weight loss curve is around 100–275 °C (14.20%) in TGA due to the elimination of the hydroxyl group and oxidative degradation of the surface-bound organic moiety. The main weight-loss step, which initiates at the onset point of 275 °C up to 350 °C in TGA and a slight endothermic event at 382 °C in DTA, corresponds to the complete degradation of magnetite doped TDI and DES molecules. By the end of

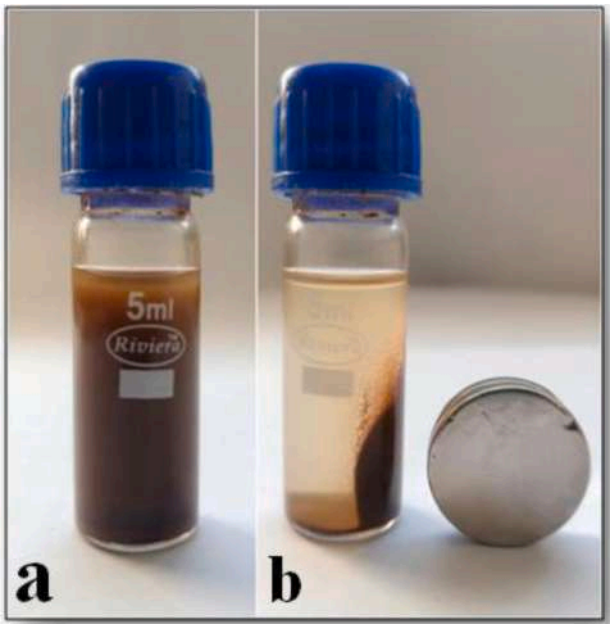

Fig. 9. Magnetic separation of the catalysts from the reaction medium.

this step, a total of 58.71% of the mass is lost from 350 °C onwards in TGA and a deep endothermic peak at 577 °C in DTA is attributed to the disintegration of carbonaceous material by removing gaseous CO_2 molecules. Finally, it is deduced that the prepared magnetic nano-catalyst Fe_3O_4@SiO_2@TDI@DES is thermally stable up to 275 °C [15, 53]. Also, we found almost same thermal behavior of the reused catalyst (Fig. 4b).

3.1.4. Energy dispersive X-ray (EDX)

The elemental status of the Fe_3O_4@SiO_2@TDI@DES sample can be investigated effectively using EDX analysis (Fig. 5). The EDX results show the presence of the expected elements Fe (15.05 w/w percent), O (30.51 w/w percent), Si (17.06 w/w percent), N (11.3 8 w/w percent), C (19.29 w/w percent), and Cl (6.71 w/w percent), indicating the nano-catalyst structure.

3.1.5. Field emission scanning electron microscopy (FE-SEM)

FE-SEM analysis was employed to study the surface morphology and particle size of Fe_3O_4@SiO_2@TDI@DES NPs. As can be seen in Fig. 6a

Table 2
Fe_3O_4@SiO_2@TDI@DES catalyzed synthesis of 2,2́-(2-oxoindoline-3–3diyl)bis (1H-indene-1,3(2*H*)-dione)[a].

Entry	R_1	R_2	Product	Time (min)	Yield[b] (%)	M.P.(°C) [Literature]
1	H	H	3a	17	95	255–257 [25a]
2	H	Br	3b	28	88	242 [25a]
3	H	F	3c	37	94	243 [25a]
4	H	NO_2	3d	20	96	227–230 [25a]
5	-CH_2Ph	H	3e	31	87	218–221 [25a]
6	H	OMe	3f	35	85	245–246 [25b]
7	H	Cl	3 g	25	91	250–252[c]
8	H	I	3h	24	93	262–264[c]
9	-CH_2PhCl	H	3i	33	90	234–236[c]
10	-CH_2PhMe	H	3j	32	86	242–244[c]

[a] Reaction conditions: isatin (1 mmol), 1,3-indendione (1 mmol), and Fe_3O_4@SiO_2@TDI@DES (15 mg) in ethanol (5 mL) at 80 °C.[b]Isolated yield. [c]Novel compound.

Table 3
Comparison of catalytic efficiency of Fe_3O_4@SiO_2@-TDI@DES with reported catalysts in the synthesis of 2,2́-(2-oxoindoline-3–3diyl)bis(1H-indene-1,3(2H)-dione).

Entry	Catalyst	Conditions	Time (min)	Yield (%)
1	Fe_3O_4	Ethanol/80 °C, Reflux	180	Trace
2	Fe_3O_4@SiO_2	Ethanol/80 °C, Reflux	180	Trace
3	*p*-TSA	EtOH/40 °C, Ultrasound	120	90
4	ChCl/ glycerol	ChCl/ glycerol, 70 °C	15	94
5	Fe_3O_4 @SiO_2@TDI@DES	Ethanol/80 °C, Reflux	17	95

Table 1
Optimization study for the synthesis of 2,2́-(2-oxoindoline-3–3diyl)bis(1H-indene-1,3(2H)-dione)[a].

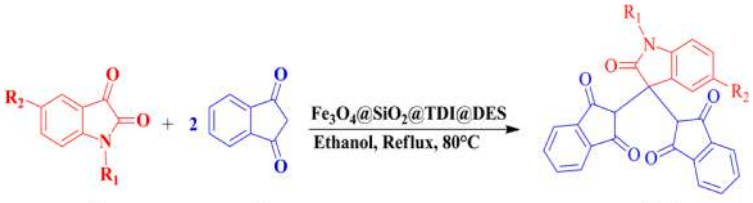

1 2 3a-j

Entry	Catalyst (mg)	Conditions	Time (min)	Yield[b](%)
1	–	H_2O/RT	120	0
2	–	Ethanol/RT	90	0
3	Fe_3O_4 @SiO_2@TDI@DES (5)	Ethanol/RT	70	74
4	Fe3O4 @SiO2@TDI@DES (5)	CH3CN/60 oC	82	47
5	Fe_3O_4 @SiO_2@TDI@DES (5)	Chloroform/60 °C	36	55
6	Fe_3O_4 @SiO_2@TDI@DES (5)	Ethyl acetate/60 °C	41	60
7	Fe_3O_4 @SiO_2@TDI@DES (5)	Toluene/60 °C	91	39
8	Fe_3O_4 @SiO_2@TDI@DES (5)	THF/60 °C	65	70
9	Fe_3O_4 @SiO_2@TDI@DES (5)	Methanol/60 °C	40	53
10	Fe_3O_4 @SiO_2@TDI@DES (5)	Acetone/60 °C	50	49
11	Fe_3O_4 @SiO_2@TDI@DES (5)	n-Hexane/60 °C	95	45
12	Fe_3O_4 @SiO_2@TDI@DES (5)	Ethanol/60 °C	57	81
13	Fe_3O_4 @SiO_2@TDI@DES (10)	Ethanol/60 °C	50	84
14	Fe_3O_4 @SiO_2@TDI@DES (15)	Ethanol/60 °C	45	88
15	Fe_3O_4 @SiO_2@TDI@DES (15)	Ethanol/80 °C	17	95
16	Fe_3O_4 @SiO_2@TDI@DES (20)	Ethanol/80 °C	17	95

[a] Reaction conditions: isatin (1 mmol), 1,3-indendione (1 mmol), and Fe_3O_4@SiO_2@TDI@DES (15 mg) in ethanol (5 mL) at 80 °C. [b]Isolated yield.

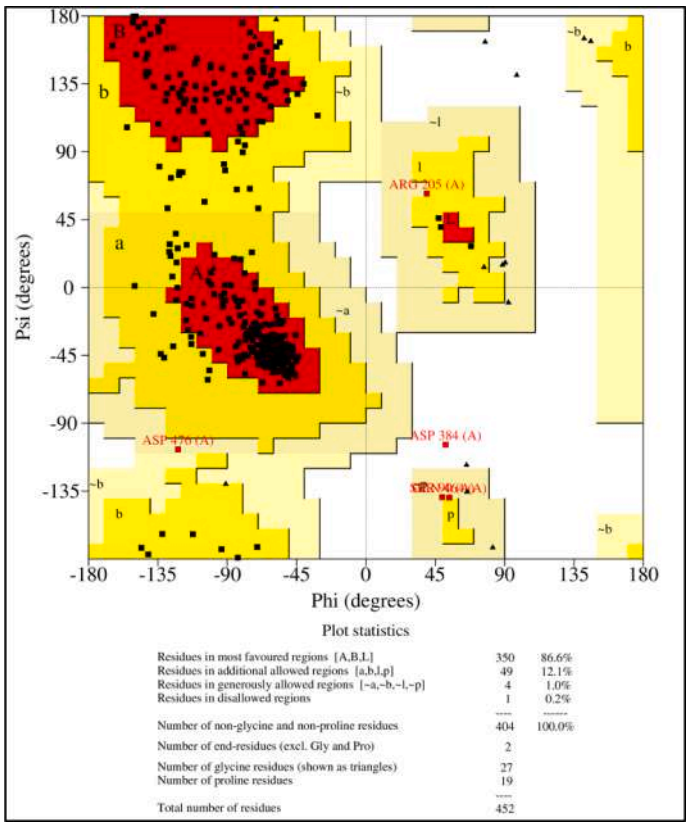

Fig. 10. Ramachandran plot of the aromatase (PDB ID: 3s79) showing 86.6% residues in the favored region.

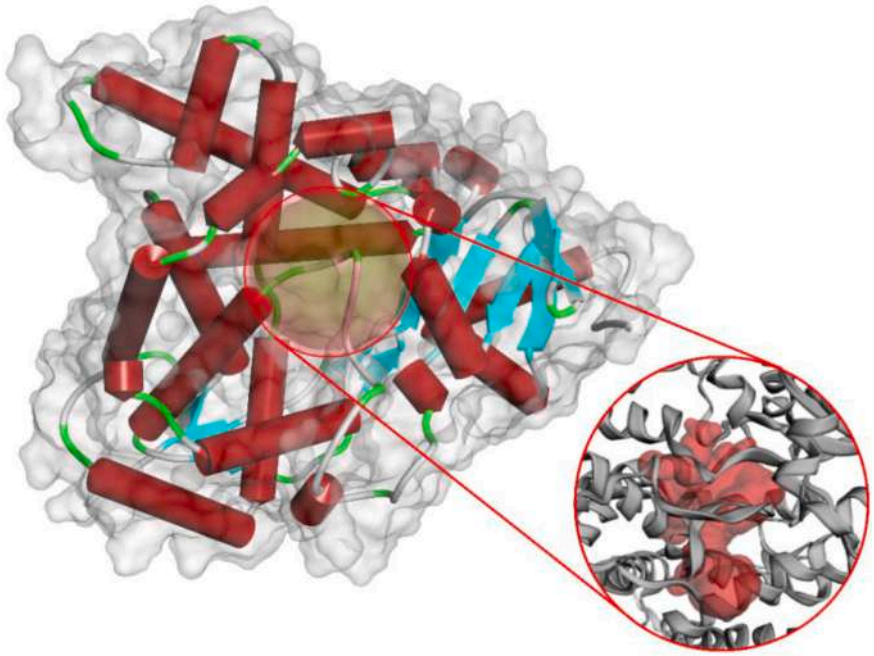

Fig. 11. Binding pocket (red) present in 3s79.

and 6b, the particles are flakes shaped in the form of clusters and reveal the transparent and core-shell morphology of the catalyst.

3.1.6. *High-resolution transmission electron microscopy (HR-TEM)*

The morphology and particle size of Fe_3O_4@SiO_2@TDI@DES was further investigated by HR-TEM. Fig. 7 (a-d) shows the high-resolution images of Fe_3O_4@SiO_2@TDI@DES nanocomposite, which reveal the uniform distribution of organic moiety on the surface of nanoparticles. The formation of the core-shell was observed around the small Fe_3O_4 nanoparticles, which is the main focus of the present report for the preparation of the core-shell nanocatalyst. Fig. 7a shows the formation of nano spherical surface morphology with an average particle size of 11

Table 4
The Binding affinity of synthesized compounds against the aromatase (PDB ID: 3s79) along with interacting residue and type of interaction.

Compound No.	Binding affinity (kcal mol^{-1})	Interacting residue	Type of interaction
3a	−10.3	LEU152, ILE133, PHE148, ALA306, ILE132, ALA438, THR310, ARG115, PHE430, VAL370, CYS437, VAL373, LEU372, LEU477, TRP224, GLY439, MET303	VDW, H Bond, Pi-Donor H Bond, Pi-Sigma, Pi-Sulfur, Pi-Alkyl
3b	−10.1	LEU152, GLY439, ASP309, PHE221, SER478, VAL370, LEU477, PHE134, ILE132, ARG435, ARG145, TRP224, ARG115, ILE133, CYS437, ALA438, THR310, ALA306, PHE148	VDW, H Bond, Pi-Pi T Shaped, Pi-Sulfur, Pi-Alkyl, Alkyl
3c	−11.2	ILE132, ALA306, PHE148, ILE133, MET303, GLU302, THR310, CYS437, ALA443, PHE430, TRP224, VAL370, PHE221, LEU477, ARG115, GLY439	VDW, Halogen, Pi-Donor H Bond, Pi-Alkyl
3d	−10.3	SER478, PHE221, VAL370, ASP309, ARG115, THR310, CYS437, PHE430, PRO429, MET364, GLY439, LEU152, PHE148, ILE132, MET303, ALA306, GLY302, ALA438, ILE133, PHE134, LEU477, TRP224	VDW, H Bond, Pi-Donor H Bond, Pi-Sigma, Pi-Sulfur, Pi-Alkyl
3e	−11.2	MET374, VAL373, PHE430, CYS437, TRP224, VAL370, THR310, SER478, PHE221, ASP309, ALA438, ILE132, ARG145, ILE133, PHE148, ALA306, MET303, LEU152, GLY439, PHE134, ARG115, LEU477	VDW, Pi-Pi T Shaped, Pi-Alkyl
3f	−10	SER478, LEU372, LEU477, TRP224, VAL370, PHE134, ILE133, GLU302, MET303, ILE132, ALA438, PHE148, LEU152, ALA306, GLY439, PRO429, CYS437, PHE430, ARG115, THR310	VDW, H Bond, Pi-Sigma, Pi-Sulfur, Pi-Alkyl, Alkyl
3 g	−10	LEU152, GLY439, ASP309, TRP224, PHE221, SER478, VAL370, LEU477, PHE134, ARG145, ILE132, ARG435, ARG115, ILE133, CYS437, THR310, ALA306, ALA438, PHE148	VDW, H Bond, Pi-Pi T Shaped, Pi-Sulfur, Pi-Alkyl, Alkyl
3h	−10.2	VAL373, CYS437, TRP224, ASP309, VAL370, PHE221, SER478, THR310, LEU477, LEU152, PHE148, ALA306, ILE132, ILE133, ALA438, PHE134, MET374, ARG115	VDW, H Bond, Pi-Cation, Pi-Alkyl
3i	−11.7	THR310, ALA307, TRP224, ALA306, PHE134, LEU477, LEU372, LEU152, PHE148, ILE132, MET374, ILE133, MET303, ALA438, VAL370, CYS437, GLY439, ARG115, VAL373, PHE430, ALA443	VDW, Pi-Donor H Bond, Pi-Sigma, Pi-Sulfur, Pi-Alkyl, Pi-Cation, Alkyl
3j	−11.9	ALA443, VAL373, ARG115, PHE430, CYS437, VAL370, GLY439, VAL370, ILE132, ALA438, MET303, ILE133, LEU152, PHE148, LEU372, LEU477, PHE134, MET374, ALA306, TRP224, ALA307, THR310	VDW, Pi-Donor H Bond, Pi-Sigma, Pi-Sulfur, Pi-Alkyl, Pi-Cation, Alkyl

nm.

3.1.7. Vibrating sample magnetometer (VSM) analysis

The magnetic properties of Fe_3O_4@SiO_2@TDI@DES nanocomposite were investigated by a vibrating sample magnetometer (VSM) at room temperature. The saturation magnetization of Fe_3O_4 (Fig. 8a) and Fe_3O_4@SiO_2@TDI@DES (Fig. 8b) are 74 emu/g and 7.4 emu/g respectively, at an applied field of 15,000 Oe (Fig. 8). VSM study of Fe_3O_4@SiO_2@TDI@DES nanocomposite shows saturation magnetization is reduced due to the covalent anchoring of organic molecules on the surface of Fe_3O_4 MNPs. Even though, it's still high enough to be separated by an external magnet as shown in Fig. 9.

3.2. Catalytic studies of novel Fe_3O_4@SiO_2@TDI@DES nanocomposite

The model reaction of 1, 3-indendione, and isatin was used to investigate optimized reaction conditions using different solvents and temperature conditions (Table 1). Initially, the model reaction under the catalyst-free condition in water and ethanol at room temperature resulted in a very poor yield of the desired **3a** (Table 1, entries 1–2). After scrutinizing, it was found that the model reaction in absolute ethanol and Fe_3O_4@SiO_2@TDI@DES (5 mg) catalyst shows the massive yield of product (**3a**) (Table 1, entry 3). Subsequently, different types of solvents were employed at high temperatures (Table 1, entries 4-12). The effect of solvent on the yield of **3a** was investigated by selecting CH_3CN, chloroform, ethyl acetate, toluene, THF, methanol, acetone, n-hexane, and ethanol (Table 1, entries 4–12). After that, we did some changes in the reaction condition and catalyst amount (Table 1, entries 13–15). The experimental results showed that the best yield of **3a** was obtained when the mixture was refluxed at 80 °C in presence of 15 mg of catalyst (Table 1, entry 15). Further, an increase in the amount of catalyst did not show an appreciable change in the product yield of **3a** (Table 1, entry 16). After optimizing reaction conditions (Table 1,

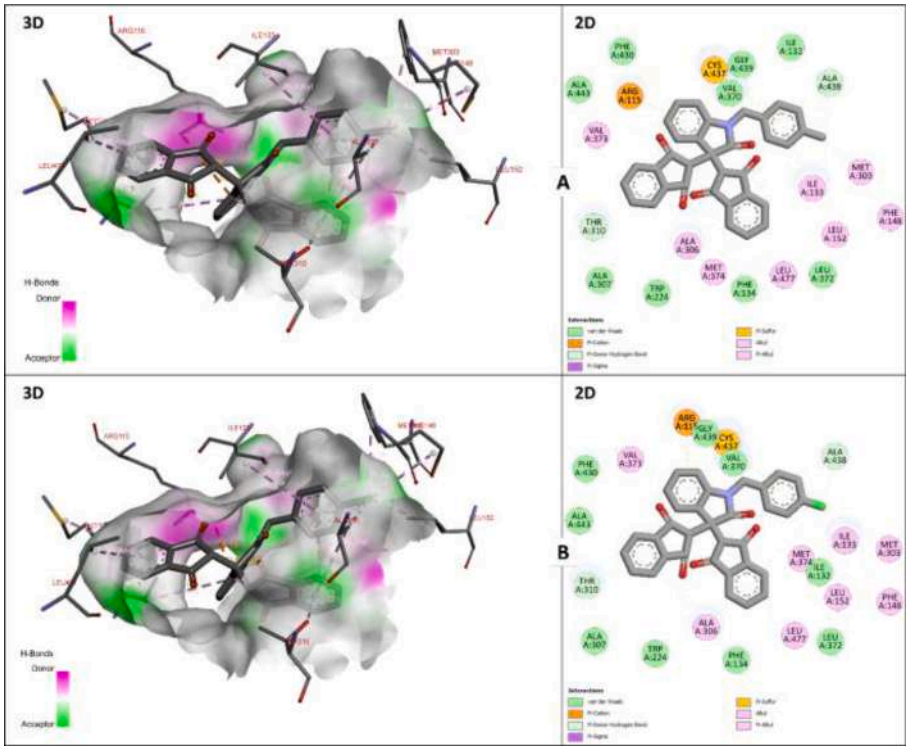

Fig. 12. 2D and 3D interaction of a) 3j and b) 3i with 3s79.

entries 1–16), the substrate scope of the protocol was examined by employing structurally diverse isatins (Table 2, entries 1–10). It was noticed that isatins with the electron-withdrawing group afforded excellent yields (Table 2, entries 2–4, 7, 8) as compared to electron-donating substituents. It was also found that this heterogeneous catalyst, Fe_3O_4@SiO_2@TDI@DES showed higher catalytic activity than the corresponding *p*-TSA and ChCl/glycerol (Table 3, entries 3–5).

3.3. Insilico studies

In silico virtual screening methods helps to increase the efficiency of the drug discovery process and reduce the experimental cost and time. Synthesized compounds were prepared for molecular docking using the free version of BIOVA Discovery Studio 2020.

Molecular docking is an established and widely applied computational tool for the prediction of correct binding modes in the interaction of protein-ligand complexes (Figs. 10 and 11). In the present study, molecular docking was done by using the AutoDockVina plugin from PyRx 0.8 software [54,44]. All synthesized compounds were docked against aromatase (PDB ID: 3s79). Table 4 revealed that the binding affinity of synthesized compounds with targeted protein ranged from −10 to −11.9 kcal mol^{-1}. Among all compounds, **3j** and **3i** showed a higher binding affinity of −11.9 kcal mol^{-1} and −11.7 kcal mol^{-1}. The free version of BIOVA Discovery Studio Visualizer 2020 was utilized for the determination of detailed interaction of best conformation. The interaction of **3j** and **3i** with residues of 3s79 showed the highest affinity interaction (Fig. 12a, b). The interacting residues and type of interaction formed between the docked compounds and the targeted macromolecule (3s79) are represented in table 4.

Drug-likeness and *in silico* ADMET studies were carried out to obtain drug-like candidates from synthesized compounds. Lipinski's rule of five is a commonly used method for the prediction of the drug-likeness of synthesized compounds. Additionally, Veber's rule, Ghose's rule, Egan's rule, and Muegge's rule were also applied to estimate the drug-likeness of compounds under study. Synthesized compounds showed acceptable drug-likeness properties showing minimum violations in Lipinski's rule of five as shown in Table 6 Pharmacokinetic ADMET (Absorption, Distribution, Metabolism, Excretion, Toxicity) characterizations were done virtually using Molinspiration, and pkCSM servers to understand the pharmacokinetic profile of synthesized compounds. It is observed that all synthesized compounds except **3d** showed good ADMET properties as shown in Table 5, 3d positive result of AMES toxicity and hence may be mutagenic. *In silico* ADMET profile of the synthesized compounds showed satisfactory results.

3.4. Molecular dynamic simulation

Dynamic behavior and configurational changes of **3j** were analyzed using the molecular dynamic (MD) simulation technique as it showed a high binding affinity with the targeted protein (PDB: 3s79). Calculation of parameters such as root mean square deviation (RMSD), root mean square fluctuation (RMSF), the radius of gyration (Rg), and the number of hydrogen bonds were done using generated trajectories from WebGro. RSMD helps to analyze the conformational stability of the protein-ligand complex system. The minimum RMSD value indicates the more conformational stability of the protein-ligand complex system. RMSD of the protein backbone and the protein-ligand complex was calculated to obtain the equilibrium time of the simulated protein-ligand complex. Fig. 13 presents the RMSD graph of the **3j** with protein backbone. Through the RMSD analysis, it is observed that the ligand showed minimum deviation in maintaining its alignment with the protein backbone over the simulation time of 100 ns. RMSF values for backbone protein and protein-ligand complex were plotted at 300 K as given in Fig. 13b.

Through the plot, it is observed that backbone fluctuations occur in PRO50, GLY51, MET54, GLU342, PRO408, PRO410, GLY433, PRO434, ARG435, GLY436, CYS437, ALA438, GLN466, ASN496 amino acid residues and in protein-ligand complex, GLY91, SER118, ASN136, GLU181, SER182, SER267, THR268, GLU269, GLU270, LYS271, LEU272, GLU273, GLU274, CYS275, MET276, LEU378, GLU379, ASP380 amino acid residues showed fluctuations. However, the RMSF values remain in the acceptable range i.e. near 0.2 nm indicating the

Table 5
Predicted *in silico* ADMET properties for synthesized compounds.

	Absorption	Metabolism	Metabolism	Metabolism	Inhibitors					Excretion	Toxicity
	Intestinal absorption (human)	VDss (human)	BBB perme ability	CNS perme ability	Substrate CYP					Total clearance	AMES toxicity
	Numeric (% absorbed)	Numeric (log L kg^{-1})	Numeric (log BB)	Numeric (log PS)	Categorical (Yes/No)					Numeric (log mL min^{-1} kg^{-1})	Catego rical (Yes/No)
					2D6	3A4	1A2	2C19	2C9	2D6	3A4		
3a	93.181	−1.157	−0.094	−2.047	No	Yes	No	Yes	Yes	No	Yes	−0.186	No
3b	94.116	−1.025	−0.289	−1.903	No	Yes	No	Yes	Yes	No	Yes	−0.266	No
3c	100	−1.252	−0.253	−2.877	No	Yes	No	Yes	Yes	No	Yes	−0.284	No
3d	82.082	−1.424	−0.526	−2.229	No	Yes	No	No	Yes	No	Yes	−0.054	Yes
3e	100	−1.57	−0.547	−1.791	No	Yes	No	Yes	Yes	No	No	−0.129	No
3f	99.003	−1.351	−0.176	−2.949	No	Yes	No	Yes	Yes	No	Yes	−0.11	No
3 g	94.38	−1.037	−0.281	−0.281	No	Yes	No	Yes	Yes	No	Yes	−0.244	No
3h	92.278	−1.015	−0.293	−1.936	No	Yes	No	Yes	Yes	No	Yes	−0.555	No
3i	100	−1.556	−0.737	−1.628	No	Yes	No	Yes	Yes	No	No	−0.191	No
3j	100	−1.552	−0.562	−1.723	No	Yes	No	Yes	Yes	No	No	−0.127	No

stability of particular amino acid residues. Rg values for aromatase (PDB: 3s79) and 3j complex were studied for 100 ns at 300 K. It is observed that the Rg values for the complex ranged between 2.22–2.25 nm and showed conformational stability of the complex with minimum fluctuation in the plot, as shown in Fig. 13c. The number of hydrogen bonds present in the complex and their consistency throughout the 100 ns simulation was analyzed at 300 K, as shown in Fig. 13d. There is not much considerable change observed in the hydrogen bond interaction within the protein-ligand complex.

3.5. Antioxidant activity

The oxygen-centered free radicals, such as superoxide, hydroxyl, and nitric oxide, are referred to as reactive oxygen species (ROS). They are produced in the human body and cause damage to lipids, proteins, and DNA, potentially leading to carcinogenesis, drug-associated toxicity, and inflammation [55]. The production of ROS by macrophages and activated neutrophils has also been linked to a variety of illnesses. Natural or synthetic anti-oxidants are compounds that engage with free radicals and interrupt their chain reactions before they destroy key important components. As a result, they have only lately been developed as medication candidates to combat these various disorders.

In this study, the antioxidant activity of synthesized compounds was determined by a DPPH scavenging assay. The reduction capacity of DPPH radicals was measured by the decrease in its absorbance at 517 nm, which is generated by antioxidants. Here all the synthesized compounds possessed promising radical scavenging activity compared with standard ascorbic acid. The highest activity was obtained for 3 g (91.42 ± 0.62%) followed by 3 h (90.77 ± 0.59%) and **3a** (90.44 ± 0.83%). Whereas the lowest activity was obtained for **3c** (74.81 ± 0.74%), and **3e** (79.07 ± 0.94%). The rest of the compounds executed good antioxidant activity. Results are depicted in Fig. 14. It is generally known that chemical compounds containing groups that donate electrons (amine, hydroxyl, and methoxy) are capable of acting as free radical trapping agents and combating oxidative stress. Here, the synthesized compounds possessing electron-withdrawing groups are responsible to scavenge the formed radicals for possessing anti-oxidant activity.

3.6. Plausible mechanism

A plausible mechanism of a one-pot pseudo-three component reaction of isatin and 1,3-indendione for the synthesis of 2,2́-(2-oxoindoline-3–3diyl)bis(1H-indene-1,3(2H)-dione) **(3a)** is proposed in Scheme 3. As illustrated in Scheme 3, in step **I** hydrogen bonding between choline chloride and oxalic acid binds with the isatin carbonyl group due to which, the electrophilicity of the carbonyl group increases. In step **II**, the catalyst abstracts the proton from the 1,3-indendione to give an intermediate. In step **III**, another molecule of catalyst reacts with an intermediate formed in step **II** to give a product **(3a)** 2,2́-(2-oxoindoline-3–3diyl)bis(1H-indene-1,3(2H)-dione) with a loss of H_2O.

3.7. Recyclability of Fe_3O_4@SiO_2@TDI@DES

The reusability of catalysts is an important criterion in the viewpoint of green chemistry applications in academic and industrial research. In this regard, the heterogeneous catalysts are promising candidates due to their facile separation, recoverability, reusability, and leaching. The reusability study of Fe_3O_4@SiO_2@TDI@DES nanocomposite was investigated using model reaction under optimized reaction conditions. After completion of the model reaction, Fe_3O_4@SiO_2@TDI@DES was recovered by an external magnet. The catalyst was washed thoroughly with ethanol and kept for drying at 60 ^{o}C for 2 h in a vacuum oven. A reusability study shows that Fe_3O_4@SiO_2@TDI@DES could be reused for five runs without significant loss of catalytic activity and product yield (Fig. 15). The procedure of isolation, washing, and drying of the catalyst was repeated after every cycle.

Table 6
Drug-likeness prediction of synthesized compounds.

Compound	Lipinski's rule of five					Lipinski's violations	Drug likeness		
	MW	iLogP	nHBA	nHBD	MR		Lipinski	Veber	Ghose
3a	421.408	2.13	5	2	117.21	0	Yes	Yes	Yes
3b	500.3	2.46	5	1	124.91	1	Yes	Yes	No
3c	439.39	2.19	6	1	117.17	0	Yes	Yes	Yes
3d	466.4	1.85	7	1	126.03	0	Yes	No	Yes
3e	511.52	2.97	5	0	146.6	1	Yes	Yes	No
3f	463.44	2	6	1	127.4	0	Yes	Yes	Yes
3 g	455.85	2.28	5	1	122.22	0	Yes	Yes	Yes
3h	547.3	2.36	5	1	129.93	1	Yes	Yes	No
3i	545.97	3.27	5	0	151.61	1	Yes	Yes	No
3j	525.55	3.15	5	0	151.56	1	Yes	Yes	No

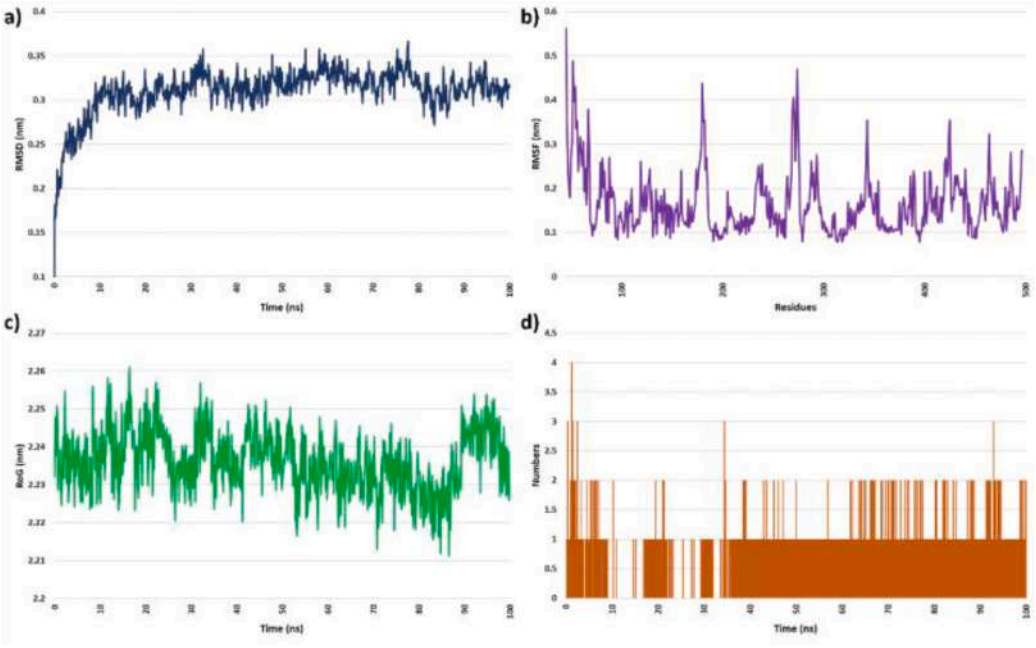

Fig. 13. a) RMSD, b) RMSF, c) Radius of gyration, and d) Hydrogen bonds for the complex between aromatase (PDB: 3s79) and 3j at 300 K for 100 ns.

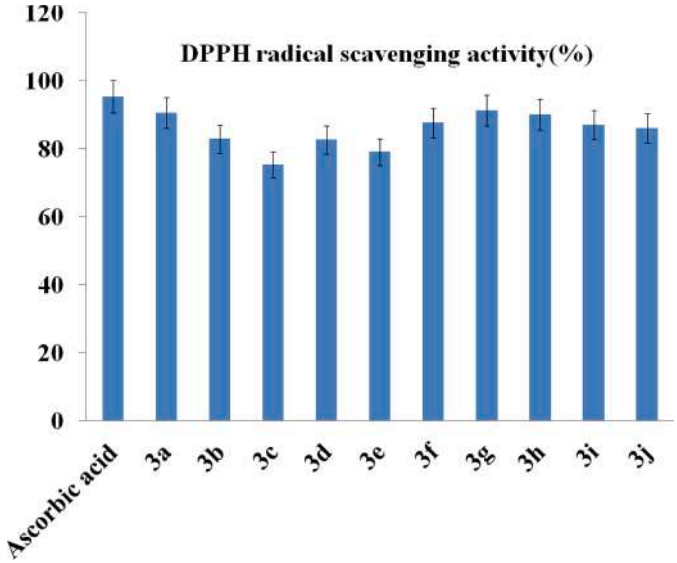

Fig. 14. DPPH radical scavenging activity of synthesized compounds at 100 μg concentration.

4. Conclusion

The present study introduced a novel and cost-effective magnetically separable Fe_3O_4@SiO_2@TDI@DES (oxalic acid: choline chloride) nano-sized catalyst that has been prepared for the first time. By using an external magnet the catalyst could be readily retrieved and reused for five cycles without losing any catalytic activity. The catalytic efficacy of novel Fe_3O_4@SiO_2@TDI@DES is demonstrated for the efficient synthesis of 2,2́-(2-oxoindoline-3–3diyl)bis(1H-indene-1,3(2H)-dione) *via* a one-pot synthesis reaction approach. The present methodology offers several benefits such as excellent yields, shorter reaction times, and an easy workup procedure. Synthesized compounds were virtually screened against aromatase (PDB: 3s79). Through the results of molecular docking, it is observed that all synthesized compounds have a good binding affinity with 3s79. All compounds successfully passed all the requirements of drug-likeness analysis and showed good ADMET properties except **3d** The molecular dynamic simulation was performed with a protein-ligand complex having high binding affinity and the RMSD, RMSF radius of gyration, and hydrogen bond were analyzed. Through the results of MD simulation, it is observed that subjected complex (3s79 + C9) was stable throughout the 100 ns simulation time.

4.1. Credit author statement

Prasad Swami: Synthesis of Catalyst, oxindoles and characterization,

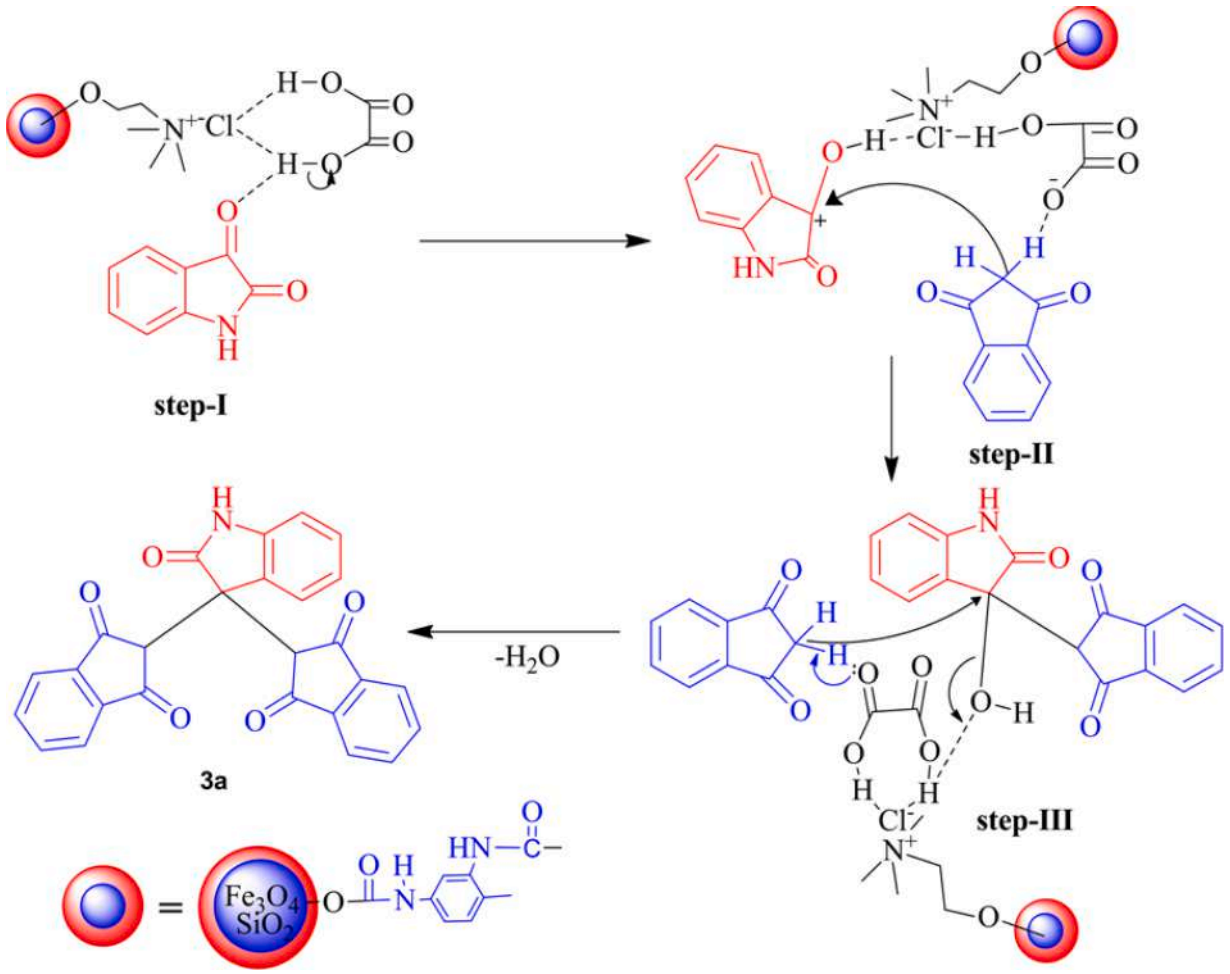

Scheme 3. Plausible mechanism for the synthesis of 2,2́-(2-oxoindoline-3–3diyl)bis(1H-indene-1,3(2H)-dione) **(3a)**.

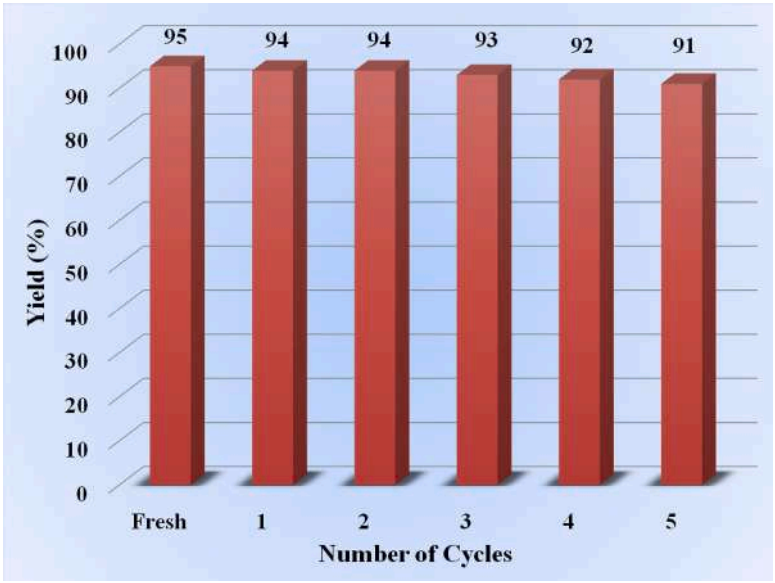

Fig. 15. Recyclability of the Fe_3O_4@SiO_2@TDI@DES catalyst.

Devashree Patil: Antioxidant activity study,
Sanket Rathod, Prafulla Choudhari**:** Docking study,
Sandeep Sankpal, Ajinkya Patravale, Yogesh Nalwar: Softwares and Concept,
Shankar Hangirgekar: Concept, referencing, manuscript writing, and editing.

Supplementary data

Scanned copies of FT-IR, ^{1}H, and ^{13}C NMR and Mass spectra of novel oxindole (3 g, 3 h, 3i, 3j) derivatives are given in supplementary information.

Declaration of Competing Interest

There are no conflicts to declare.

Data availability

Data will be made available on request.

Acknowledgments

The author Prasad Swami is thankful to the Government of Maharashtra Other Backward Bahujan Welfare Department, Maharashtra State, Mumbai for providing Mahatma Jyotiba Phule Research Fellowship (MJPRF) Outward No. MAHAJYOTI/Nag./Fellowship/2021–22/1042(324).

Supplementary materials

Supplementary material associated with this article can be found, in the online version, at doi:10.1016/j.molstruc.2023.136079.

References

[1] K. Alfonsi, J. Colberg, P.J. Dunn, T. Fevig, S. Jennings, T.A. Johnson, H.P. Kleine, C. Knight, M.A. Nagy, D.A. Perry, M. Stefaniak, Green chemistry tools to influence a medicinal chemistry and research chemistry based organisation, Green Chem. 10 (2008) 31–36, https://doi.org/10.1039/b711717e.

[2] O.V. Kharissova, B.I. Kharisov, C.M.O. González, Y.P. Méndez, I. López, Greener synthesis of chemical compounds and materials, 2019. 10.1098/rsos.191378.

[3] (a) D. Lenoir, K.W. Schramm, J.O. Lalah, Green Chemistry: some important forerunners and current issues, Sustain. Chem. Pharm. 18 (2020), 100313, https://doi.org/10.1016/j.scp.2020.100313;
(b) Y. Cui, W. Kang, L. Qin, J. Ma, X. Liu, Y. Yang, Ultrafast synthesis of magnetic hollow carbon nanospheres for the adsorption of quinoline from coking wastewater, New J. Chem. 44 (2020) 7490–7500, https://doi.org/10.1039/d0nj00944j.

[4] T.J. Collins, Review of the twenty-three year evolution of the first university course in green chemistry: teaching future leaders how to create sustainable societies, J. Clean. Prod. 140 (2017) 93–110, https://doi.org/10.1016/j.jclepro.2015.06.136.

[5] H. Duan, D. Wang, Y. Li, Green chemistry for nanoparticle synthesis, Chem. Soc. Rev. 44 (2015) 5778–5792, https://doi.org/10.1039/c4cs00363b.

[6] M.T. White, G. Bianchi, L. Chai, S.A. Tassou, A.I. Sayma, Review of supercritical CO2 technologies and systems for power generation, Appl. Therm. Eng. 185 (2021), 116447, https://doi.org/10.1016/j.applthermaleng.2020.116447.

[7] S. Khandelwal, Y.K. Tailor, M. Kumar, Deep eutectic solvents (DESs) as eco-friendly and sustainable solvent/catalyst systems in organic transformations, J. Mol. Liq. 215 (2016) 345–386, https://doi.org/10.1016/j.molliq.2015.12.015.

[8] (a) P.P. Mohire, D.R. Chandam, A.A. Patravale, P. Choudhari, V. Karande, J. S. Ghosh, M.B. Deshmukh, An Expedient Four Component Synthesis of Substituted Pyrido-Pyrimidine Heterocycles in Glycerol:proline Based Low Transition Temperature Mixture and Their Antioxidant Activity with Molecular Docking Studies, Polycycl. Aromat. Compd. 42 (2021) 137–155, https://doi.org/10.1080/10406638.2020.1720749;
(b) D.R. Chandam, A.A. Patravale, S.D. Jadhav, M.B. Deshmukh, Low melting oxalic acid dihydrate: proline mixture as dual solvent/catalyst for synthesis of spiro [indoline-3,9′-xanthene]trione and dibarbiturate derivatives, J. Mol. Liq. 240 (2017) 98–105, https://doi.org/10.1016/j.molliq.2017.05.070.

[9] C.J. Clarke, W.C. Tu, O. Levers, A. Bröhl, J.P. Hallett, Green and Sustainable Solvents in Chemical Processes, Chem. Rev. 118 (2018) 747–800, https://doi.org/10.1021/acs.chemrev.7b00571.

[10] R. Xin, S. Qi, C. Zeng, F.I. Khan, B. Yang, Y. Wang, A functional natural deep eutectic solvent based on trehalose: structural and physicochemical properties, Food Chem. 217 (2017) 560–567, https://doi.org/10.1016/j.foodchem.2016.09.012.

[11] D.V. Wagle, H. Zhao, G.A. Baker, ChemInform Abstract: deep Eutectic Solvents: sustainable Media for Nanoscale and Functional Materials, ChemInform. 45 (2014) no-no. 10.1002/chin.201441292.

[12] (a) P. Liu, J.W. Hao, L.P. Mo, Z.H. Zhang, Recent advances in the application of deep eutectic solvents as sustainable media as well as catalysts in organic reactions, RSC Adv. 5 (2015) 48675–48704, https://doi.org/10.1039/c5ra05746a;
(b) Y. Riadi, Green, rapid and efficient synthesis of new antibacterial pyridopyrimidinone mediated by eutectic mixture of Urea/CuCl2, Sustain. Chem. Pharm. 15 (2020), 100233, https://doi.org/10.1016/j.scp.2020.100233.

[13] (a) N. Fu, L. Li, K. Liu, C.K. Kim, J. Li, T. Zhu, J. Li, B. Tang, A choline chloride-acrylic acid deep eutectic solvent polymer based on Fe_3O_4 particles and MoS_2 sheets (poly(ChCl-AA DES)@Fe_3O_4@MoS_2) with specific recognition and good antibacterial properties for β-lactoglobulin in milk, Talanta 197 (2019) 567–577, https://doi.org/10.1016/j.talanta.2019.01.072;
(b) S. Molaei, N. Moeini, M. Ghadermazi, Synthesis of CoFe2O4 @Amino glycol/Gdnanocomposite as a high-efficiency and reusable nanocatalyst for green oxidation of sulfides and synthesis of 5-substituted 1H-tetrazoles, J. Organomet. Chem. 977 (2022), 122459, https://doi.org/10.1016/j.jorganchem.2022.-122459.

[14] (a) A. Sápi, T. Rajkumar, J. Kiss, Á. Kukovecz, Z. Kónya, G.A. Somorjai, Metallic Nanoparticles in Heterogeneous Catalysis, Catal. Lett. 151 (2021) 2153–2175, https://doi.org/10.1007/s10562-020-03477-5;
(b) S. Shylesh, V. Schünemann, W.R. Thiel, Magnetically separable nanocatalysts: bridges between homogeneous and heterogeneous catalysis, Angew. Chemie - Int. Ed. 49 (2010) 3428–3459, https://doi.org/10.1002/anie.200905684;
(c) N. Moeini, S. Molaei, M. Ghadermazi, Selective oxidation of sulfides and synthesis, Res. Chem. Intermed. 48 (2022) 3109–3128, https://doi.org/10.1007/s11164-022-04742-5.

[15] (a) J. Safaei-Ghomi, F. Eshteghal, H. Shahbazi-Alavi, Novel ionic liquid supported on Fe_3O_4 nanoparticles as an efficient catalyst for the synthesis of new chromenes, Appl. Organomet. Chem. 32 (2018) 1–8, https://doi.org/10.1002/aoc.3987.(b)S. Molaei, M. Ghadermazi, N. Moeini, Fabrication of La (III) supported on CoFe2O4 MNPs: a novel and efficient heterogeneous catalyst for selective oxidation of sulfides and synthesis of symmetrical disulfides, 48 (2022) 771–793. 10.1007/s11164-021-04629-x.

[16] (a) J.N. Zhang, X.H. Yang, W.J. Guo, B. Wang, Z.H. Zhang, Magnetic Metal-Organic Framework $CoFe_2O_4$@SiO_2@IRMOF-3 as an Efficient Catalyst for One-Pot Synthesis of Functionalized Dihydro-2-oxopyrroles, Synlett 28 (2017) 734–740, https://doi.org/10.1055/s-0036-1588924;
(b) N. Moeini, S. Molaei, M. Ghadermazi, Dysprosium (III) Supported on CoFe2O4 MNPs as a Heterogeneous Catalyst for the Selective Oxidation of Sulfides and Synthesis of Symmetrical Disulfides, J. Mol. Struct. 1246 (2021), 131071, https://doi.org/10.1016/j.molstruc.2021.131071.

[17] (a) N. Lotfifar, A. Zare, G.Rezanejade Bardajee, Nano-[Fe_3O_4@SiO_2-R-$NHMe_2$][H_2PO_4] as a Highly Effectual and Magnetically Recyclable Catalyst for the Preparation of bis(6-Amino-1,3-dimethyluracil-5-yl)methanes under Solvent-Free Conditions, Org. Prep. Proced. Int. 53 (2021) 379–386, https://doi.org/10.1080/00304948.2021.1914487;
(b) Q. Zhang, X. Yang, J. Guan, Applications of Magnetic Nanomaterials in Heterogeneous Catalysis, ACS Appl. Nano Mater. 2 (2019) 4681–4697, https://doi.org/10.1021/acsanm.9b00976.

[18] (a) Y.M. Khetmalis, M. Shivani, S. Murugesan, K.V.G. Chandra Sekhar, Oxindole and its derivatives: a review on recent progress in biological activities, Biomed. Pharmacother. 141 (2021), 111842, https://doi.org/10.1016/j.biopha.2021.111842;
(b) G. Cerchiaro, A.M.D.C. Ferreira, Oxindoles and copper complexes with oxindole-derivatives as potential pharmacological agents, J. Braz. Chem. Soc. 17 (2006) 1473–1485, https://doi.org/10.1590/S0103-50532006000800003.

[19] A.A. El-Gendy, A.M. Ahmedy, Synthesis and Antimicrobial Activity of some New 2-indolinone Derived Oximes and Spiro-isoxazolines, Arch. Pharm. Res. 23 (2000) 310–314, https://doi.org/10.1007/BF02975439.

[20] S. Chander, C.R. Tang, A. Penta, P. Wang, D.P. Bhagwat, N. Vanthuyne, M. Albalat, P. Patel, S. Sankpal, Y.T. Zheng, M. Sankaranarayanan, Hit optimization studies of 3-hydroxy-indolin-2-one analogs as potential anti-HIV-1 agents, Bioorg. Chem. 79 (2018) 212–222, https://doi.org/10.1016/j.bioorg.2018.04.027.

[21] S. Yagnam, E. Rami Reddy, R. Trivedi, N.V. Krishna, L. Giribabu, B. Rathod, R. S. Prakasham, B. Sridhar, 1,2,3-Triazole derivatives of 3-ferrocenylidene-2-oxindole: synthesis, characterization, electrochemical and antimicrobial evaluation, Appl. Organomet. Chem. 33 (2019) 1–15, https://doi.org/10.1002/aoc.4817.

[22] M. Yousuf, D. Mukherjee, S. Dey, S. Chatterjee, A. Pal, B. Sarkar, C. Pal, S. Adhikari, Synthesis and biological evaluation of polyhydroxylated oxindole derivatives as potential antileishmanial agent, Bioorg. Med. Chem. Lett. 28 (2018) 1056–1062, https://doi.org/10.1016/j.bmcl.2018.02.023.

[23] Y. Hirata, Y. Ito, M. Takashima, K. Yagyu, K. Oh-Hashi, H. Suzuki, K. Ono, K. Furuta, M. Sawada, Novel Oxindole-Curcumin Hybrid Compound for Antioxidative Stress and Neuroprotection, ACS Chem. Neurosci. 11 (2020) 76–85, https://doi.org/10.1021/acschemneuro.9b00619.

[24] (a) Z. Song, C.P. Chen, J. Liu, X. Wen, H. Sun, H. Yuan, Design, synthesis, and biological evaluation of (2E)-(2-oxo-1, 2-dihydro-3H-indol-3-ylidene)acetate derivatives as anti-proliferative agents through ROS-induced cell apoptosis, Eur. J. Med. Chem. 124 (2016) 809–819, https://doi.org/10.1016/j.ejmech.2016.09.005;
(b) M. Kaur, M. Singh, N. Chadha, O. Silakari, Oxindole: A Chemical Prism Carrying Plethora of Therapeutic Benefits, Elsevier Ltd, 2016, https://doi.org/10.1016/j.ejmech.2016.08.011.

[25] (a) R. Ghahremanzadeh, F. Fereshtehnejad, P. Mirzaei, A. Bazgir, Ultrasound-assisted synthesis of 2,2′-(2-oxoindoline-3,3-diyl)bis(1H-indene-1,3(2H)-dione) derivatives, Ultrason. Sonochem. 18 (2011) 415–418, https://doi.org/10.1016/j.ultsonch.2010.07.010;
(b) J.S. Yadav, B.V. SubbaReddy, K.U. Gayathri, S. Meraj, A.R. Prasad, Bismuth (III) triflate catalyzed condensation of isatin with indoles and pyrroles: a facile synthesis of 3,3-diindolyl- and 3,3-dipyrrolyl oxindoles, Synthesis (Stuttg) 24 (2006) 4121–4123, https://doi.org/10.1055/s-2006-950373;

(c) L. Xu, W.H. Zhang, Z. Cui, Z. Zhang, Choline Chloride/Glycerol Promoted Synthesis of 3,3-Disubstituted Indol- 2-ones, Curr. Organocatal. 8 (2021) 249–257, https://doi.org/10.2174/2213337207999210104223005.
[26] X. Sun, M. Sui, G. Cui, L. Li, X. Li, X. Lv, F. Wu, G. Gu, Fe_3O_4 nanoparticles decorated on a CuS platelet-based sphere: a popcorn chicken-like heterostructure as an ideal material against electromagnetic pollution, RSC Adv. 8 (2018) 17489–17496, https://doi.org/10.1039/c8ra03015d.
[27] Z. Yang, H. Li, C. Liao, J. Zhao, S. Feng, P. Li, X. Liu, J. Yang, K. Shih, Magnetic Rattle-Type Fe_3O_4@CuS Nanoparticles as Recyclable Sorbents for Mercury Capture from Coal Combustion Flue Gas, ACS Appl. Nano Mater. 1 (2018) 4726–4736, https://doi.org/10.1021/acsanm.8b00948.
[28] M.A. Habila, Z.A. Alothman, A.M. El-Toni, J.P. Labis, M. Soylak, Synthesis and application of Fe_3O_4@SiO_2@TiO_2 for photocatalytic decomposition of organic matrix simultaneously with magnetic solid phase extraction of heavy metals prior to ICP-MS analysis, Talanta 154 (2016) 539–547, https://doi.org/10.1016/j.talanta.2016.03.081.
[29] M. Gao, W. Li, J. Dong, Z. Zhang, B. Yang, Synthesis and Characterization of Superparamagnetic Fe₃O₄ @SiO₂ Core-Shell Composite Nanoparticles, World J. Condens. Matter Phys. 01 (2011) 49–54, https://doi.org/10.4236/wjcmp.2011.12008.
[30] B. Ou, D. Li, Q. Liu, Z. Zhou, B. Liao, Functionalized TiO_2 nanoparticle containing isocyanate groups, Mater. Chem. Phys. 135 (2012) 1104–1107, https://doi.org/10.1016/j.matchemphys.2012.06.027.
[31] R. Verma, M. Mohan, V.V. Goud, T. Banerjee, Operational Strategies and Comprehensive Evaluation of Menthol Based Deep Eutectic Solvent for the Extraction of Lower Alcohols from Aqueous Media, ACS Sustain. Chem. Eng. 6 (2018) 16920–16932, https://doi.org/10.1021/acssuschemeng.8b04255.
[32] S. Taghavi, A. Amoozadeh, F. Nemati, Deep eutectic solvent-assisted synthesis of highly efficient nanocatalyst (n-TiO_2@TDI@DES ($ZnCl_2$:urea)) for chemoselective oxidation of sulfides to sulfoxides, Appl. Organomet. Chem. 35 (2021) 1–12, https://doi.org/10.1002/aoc.6127.
[33] V. Shah, J. Bhaliya, G.M. Patel, In silico docking and ADME study of deketenecurcumin derivatives (DKC) as an aromatase inhibitor or antagonist to the estrogen-alpha positive receptor (Erα+): potent application of breast cancer, Struct. Chem. 33 (2022) 571–600, https://doi.org/10.1007/s11224-021-01871-2.
[34] B.A. Roman Laskowski, M.W. Macarthur, J.M. Thornton, Computer Programs PROCHECK: a program to check the stereochemical quality of protein structures, J. Appl. Cryst. 26 (1993) 283–291, https://doi.org/10.1107/S0021889892009944.
[35] W. Tian, C. Chen, X. Lei, J. Zhao, J. Liang, CASTp 3.0: computed atlas of surface topography of proteins, Nucleic Acids Res. 46 (2018) 363–367, https://doi.org/10.1093/nar/gky473.
[36] A.S. Jain, P. Sushma, C. Dharmashekar, M.S. Beelagi, S.K. Prasad, C. Shivamallu, A. Prasad, A. Syed, N. Marraiki, K.S. Prasad, In silico evaluation of flavonoids as effective antiviral agents on the spike glycoprotein of SARS-CoV-2, Saudi J. Biol. Sci. 28 (2021) 1040–1051, https://doi.org/10.1016/j.sjbs.2020.11.049.
[37] A. Daina, O. Michielin, V. Zoete, SwissADME: a free web tool to evaluate pharmacokinetics, drug-likeness and medicinal chemistry friendliness of small molecules OPEN, Sci. Rep. 7 (2017) 42717, https://doi.org/10.1038/srep42717.
[38] D.E. v Pires, T.L. Blundell, D.B. Ascher, U.K. 1 Ga, pkCSM: predicting Small-Molecule Pharmacokinetic and Toxicity Properties Using Graph-Based Signatures, In Silico and Molecular Docking Studies of Black Pepper Phyto-Constituents against, EmrD Efflux Pump of E. Coli. 58 (2015) 4066–4072, https://doi.org/10.1021/acs.jmedchem.5b00104.
[39] H. Hadni, M. Elhallaoui, 2D and 3D-QSAR, molecular docking and ADMET properties: in silico studies of azaaurones as antimalarial agents, N. J. Chem. 44 (2020) 6553–6565, https://doi.org/10.1039/c9nj05767f.
[40] Z. Ya'u Ibrahim, A. Uzairu, G. Shallangwa, S. Abechi, Molecular docking studies, drug-likeness, and in-silico ADMET prediction of some novel β-Amino alcohol grafted 1,4,5-trisubstituted 1,2,3-triazoles derivatives as elevators of p53 protein levels, Sci. Afr. 10 (2020), https://doi.org/10.1016/j.sciaf.2020.e00570.
[41] Y. Isyaku, A. Uzairu, S. Uba, Computational studies of a series of 2-substituted phenyl-2-oxo-, 2-hydroxyl- and 2-acylloxyethylsulfonamides as potent anti-fungal agents, Heliyon 6 (2020), https://doi.org/10.1016/j.heliyon.2020.e03724.
[42] A. Kuriata, A.M. Gierut, T. Oleniecki, M.P. Ciemny, A. Kolinski, M. Kurcinski, S. Kmiecik, CABS-flex 2.0: a web server for fast simulations of flexibility of protein structures, Nucleic Acids Res. 46 (2018) W338–W343, https://doi.org/10.1093/nar/gky356.
[43] WebGro | UAMS, (n.d.). https://simlab.uams.edu/(accessed May 22, 2022).
[44] L. Pol-Fachin, C.L. Fernandes, H. Verli, GROMOS96 43a1 performance on the characterization of glycoprotein conformational ensembles through molecular dynamics simulations, Carbohydr. Res. 344 (2009) 491–500, https://doi.org/10.1016/j.carres.2008.12.025.
[45] A.W. Schüttelkopf, D.M.F. van Aalten, PRODRG: a tool for high-throughput crystallography of protein-ligand complexes, ActaCrystallograph. Sect. D Biol. Crystallograph. 60 (2004) 1355–1363, https://doi.org/10.1107/S0907444904011679.
[46] D.N. Patil, S.R. Yadav, S. Patil, V.A. Bapat, J.P. Jadhav, Multidimensional Studies of Pancratium parvum Dalzell Against Acetylcholinesterase: a Potential Enzyme for Alzheimer's Management, J. Am. Coll. Nutr. 39 (2020) 601–618, https://doi.org/10.1080/07315724.2019.1709914.
[47] (a) F. Liu, F. Niu, N. Peng, Y. Su, Y. Yang, Synthesis, characterization, and application of Fe_3O_4@SiO_2-NH_2 nanoparticles, RSC Adv. 5 (2015) 18128–18136, https://doi.org/10.1039/c4ra15968c;
(b) H. Li, J. Wang, Y. Li, Y. Zhao, Y. Tian, I. Kurmanbayeva, Z. Bakenov, Hierarchical sandwiched Fe3O4@C/Graphene composite as anode material for lithium-ion batteries, J. Electroanal. Chem. 847 (2019), 113240, https://doi.org/10.1016/j.jelechem.2019.113240.
[48] (a) G.H. Du, Z.L. Liu, X. Xia, Q. Chu, S.M. Zhang, Characterization and application of Fe_3O_4/SiO $_2$ nanocomposites, J. Sol-Gel Sci. Technol. 39 (2006) 285–291, https://doi.org/10.1007/s10971-006-7780-5;
(b) H. Mao, F. Cheng, C. Lei, Z. Feng, Q. Wang, B. Chu, Y. Kong, Y. Tao, C. Yao, S. Zuo, Hydrothermal Fabrication of Fe3O4@Carbonaceous Microspheres for Efficient Removal of Oil and Metal Ions from the Aqueous Phase, Ind. Eng. Chem. Res. (2019), https://doi.org/10.1021/acs.iecr.9b03415.
[49] (a) F. Xue, Y. Dong, P. Hu, Y. Deng, Y. Wei, Ethylenediamine-functionalized magnetic Fe_3O_4@SiO_2 nanoparticles: cooperative trifunctional catalysis for selective synthesis of nitroalkenes, RSC Adv. 5 (2015) 73684–73691, https://doi.org/10.1039/c5ra11798d;
(b) C. Xiang, Y. Liu, Y. Yin, P. Huang, Y. Zou, M. Fehse, Z. She, F. Xu, D. Banerjee, D. Hermida Merino, A. Longo, H.B. Kraatz, D.F. Brougham, B. Wu, L. Sun, Facile Green Route to Ni/Co Oxide Nanoparticle Embedded 3D Graphitic Carbon Nanosheets for High Performance Hybrid Supercapacitor Devices, ACS Appl. Energy Mater. 2 (2019) 3389–3399, https://doi.org/10.1021/acsaem.9b00202.
[50] S. Bo, X. Liu, Z. Zhen, Preparation and luminescence properties of hybrid materials containing lanthanide complexes covalently bonded to a terpyridine-functionalized silica matrix, J. Lumin. 128 (2008) 1725–1730, https://doi.org/10.1016/j.jlumin.2008.03.020.
[51] (a) X. Sun, L. Xu, W. Jiang, Y. Xuan, W. Lu, Z. Li, S. Yang, Z. Gu, Adsorption mechanism of rhein-coated Fe_3O_4 as magnetic adsorbent based on low-field NMR, Environ. Sci. Pollut. Res. 28 (2021) 1052–1060, https://doi.org/10.1007/s11356-020-10541-5;
(b) N. Moeini, M. Ghadermazi, S. Molaei, Synthesis and characterization of magnetic Fe3O4@Creatinine@Zr nanoparticles as novel catalyst for the synthesis of 5-substituted 1H-tetrazoles in water and the selective oxidation of sulfides with classical and ultrasonic methods, J. Mol. Struct. 1251 (2022), 131982, https://doi.org/10.1016/j.molstruc.2021.131982.
[52] (a) M. Shao, F. Ning, J. Zhao, M. Wei, D.G. Evans, X. Duan, Preparation of Fe_3O_4@SiO_2@layered double hydroxide core-shell microspheres for magnetic separation of proteins, J. Am. Chem. Soc. 134 (2012) 1071–1077, https://doi.org/10.1021/ja2086323;
(b) S. Molaei, M. Ghadermazi, N. Moeini, Selectivity adjustment of Fe3O4 MNPs based silver catalyst in oxidation of sulfides with classical and ultrasonic methods and synthesis of 5-substituted 1H-tetrazoles from aryl nitriles in water, Appl. Surf. Sci. Adv. 7 (2022), 100192, https://doi.org/10.1016/j.apsadv.2021.100192.
[53] S. Taghavi, A. Amoozadeh, F. Nemati, The first report of deep eutectic solvent (DES) nano-photocatalyst (n-TiO_2-P25@TDI@DES (urea: znCl2)) and its application on selective oxidation of benzyl alcohols to benzaldehydes, J. Chem. Technol. Biotechnol. 96 (2021) 384–393, https://doi.org/10.1002/jctb.6550.
[54] J. Eberhardt, D. Santos-Martins, A.F. Tillack, S. Forli, AutoDockVina 1.2.0: new Docking Methods, Expanded Force Field, and Python Bindings, J. Chem. Inf. Model. 61 (2021) 3891–3898, https://doi.org/10.1021/acs.jcim.1c00203.
[55] (a) K.N. Mohana, C.B.P. Kumar, Synthesis and Antioxidant Activity of 2-Amino-5-methylthiazol Derivatives Containing 1,3,4-Oxadiazole-2-thiol Moiety, ISRN Org. Chem. 2013 (2013) 1–8, https://doi.org/10.1155/2013/620718;
(b) R. Gurav, S.K. Surve, S. Babar, P. Choudhari, D. Patil, V. More, S. Sankpal, S. Hangirgekar, Rust-derived Fe_2O_3nanoparticles as a green catalyst for the one-pot synthesis of hydrazinyl thiazole derivatives, Org. Biomol. Chem. 18 (2020) 4575–4582, https://doi.org/10.1039/d0ob00109k.